Inorganic Chemistry Communications 177 (2025) 114283

Contents lists available at ScienceDirect

Inorganic Chemistry Communications

journal homepage: www.elsevier.com/locate/inoche

Research Article

Nickel(II)-thiosemicarbazone supramolecular synthons in the assembly of π–stacked infinite columns: Synthesis, spectral, structural, computational and docking studies

Ceyhun Kucuk [a,*], Elif Avcu Altıparmak [b], Sibel Celik [c], Işın Kılıç-Cıkla [d], Namık Özdemir [e], Tülay Bal-Demirci [b]

[a] Ahmet Erdogan Vocational School of Health Services, Zonguldak Bulent Ecevit University, Zonguldak, Turkey
[b] Department of Chemistry, Engineering Faculty, Istanbul University-Cerrahpaşa, 34320 Istanbul, Turkey
[c] Vocational School of Health Services, Kırsehir Ahi Evran University, 40100 Kırşehir, Turkey
[d] Department of General Secretary, Ondokuz Mayıs University, 55139 Samsun, Turkey
[e] Department of Physics, Faculty of Science, Ondokuz Mayıs University, 55139 Samsun, Turkey

ARTICLE INFO

Keywords:
Thiosemicarbazone
Nickel(II)
FMO
X-ray
DFT
Molecular docking

ABSTRACT

The complexes with the new Ni(II) ion, coordinated through O,N,N,O-donor atoms from the dibasic isothiosemicarbazone ligand, which has recently attracted special attention among a wide range of biologically active substances, were synthesized, and their structures were explained using the XRD, FT-IR, and UV–Vis spectroscopy as well as theoretical calculation methods. The single-crystal X-ray diffraction studies confirmed the formation of in the form of a distorted square-planar coordination. These complexes are mainly stabilized by π···π stacking interactions in their crystal structures. Also, the electronic properties (frontier molecular orbitals, molecular electrostatic potential, charge analyses, and Fukui functions) of complexes were determined for optimized structures by theoretical calculation methods. Topological studies were carried out with the Multiwfn program to determine the basic binding sites and weak interactions of the complexes. In the last part of the study, molecular docking studies were performed to investigate whether the synthesized complexes could be used as lung and breast cancer agents. The obtained results show that these two newly synthesized complexes can be evaluated as anticancer agents.

1. Introduction

Thiosemicarbazones, consisting of hydrazino nitrogens (N^1 and N^2), amino nitrogen (N^4), and thiocarbonyl sulfur (S), are multidentate ligands obtained through the condensation of thiosemicarbazide with aldehydes or ketones [1]. The thiosemicarbazone structure can be further functionalized by introducing various alkyl, aryl groups, and variable substituent groups (R^1, R^2, R^3, R^4, R^5), through the thiol and amino groups ($R^1R^2CH{=}N^1\text{-}N^2{=}C\text{-}(SR^3)\text{-}N^4(R^4)(R^5)$) [2,3]. The lone pair of electrons on the nitrogen imparts basic character to the imine group. Due to the nucleophilic properties of the nitrogen atom in the molecule, thione-thiol tautomerism occurs in these compounds. The tautomeric behavior of the compound can be influenced by factors such as pH, temperature, and solvent, which determine whether the structure exhibits anionic, cationic, or neutral characteristics during complex formation [4,5]. Thiosemicarbazones demonstrate versatile ligand behaviors influenced by the nature and position of their substituent groups, as well as the type and oxidation state of the metal atom [6–14]. These compounds and their metal complexes exhibit a broad range of biological activities and represent a highly significant class of compounds in pharmaceutical chemistry [15–27]. These compounds also have applications in sensors, dyes, nonlinear optics, supercapacitors, qualitative and quantitative analytical reagents, and catalysis [28–33].

Isothiosemicarbazones are structures formed when alkyl and aryl halides attach to the thiolic sulfur atom of the thiosemicarbazones. In these structures, because of the alkylation of the sulfur atom, the isothiosemicarbazones coordinate to a metal atom via the terminal nitrogen atom instead of the sulfur, thereby altering the molecular geometry [34–37]. These ligands exhibit a broad range of biological activities, particularly anticancer activity [38–40]. The biological activities of

* Corresponding author.
E-mail address: ceyhun.kucuk@beun.edu.tr (C. Kucuk).

https://doi.org/10.1016/j.inoche.2025.114283
Received 20 January 2025; Received in revised form 28 February 2025; Accepted 4 March 2025
Available online 15 March 2025

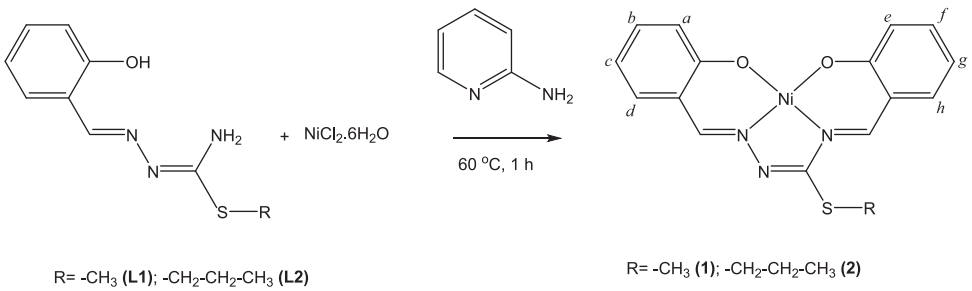

Scheme 1. Synthesis of the compounds.

Table 1
Crystal data and structure refinement parameters for **1** and **2**.

Parameters	1	2
CCDC depository	2124811	2124812
Color/shape	Dark red/rod	Dark red/prism
Chemical formula	$[Ni(C_{16}H_{13}N_3O_2S)]$	$[Ni(C_{18}H_{17}N_3O_2S)]$
Formula weight	370.06	398.11
Temperature (K)	296(2)	296(2)
Wavelength (Å)	0.71073 Mo Kα	0.71073 Mo Kα
Crystal system	Monoclinic	Monoclinic
Space group	$P2_1/n$ (No. 14)	$P2_1/n$ (No. 14)
Unit cell parameters		
a, b, c (Å)	11.3096(12), 7.9228(6), 18.0953(18)	10.9958(12), 7.8645(7), 20.955(2)
α, β, γ (°)	90, 106.465(8), 90	90, 104.348(8), 90
Volume (Å^3)	1554.9(3)	1755.6(3)
Z	4	4
$D_{calc.}$ (g/cm^3)	1.581	1.506
μ (mm^{-1})	1.394	1.240
Absorption correction	Integration	Integration
$T_{min.}$, $T_{max.}$	0.6914, 0.9714	0.6969, 0.9185
F_{000}	760	824
Crystal size (mm^3)	0.50 × 0.14 × 0.02	0.48 × 0.19 × 0.07
Diffractometer/ measurement method	STOE IPDS II/ω scan	STOE IPDS II/ω scan
Index ranges	$-13 \le h \le 13$, $-9 \le k \le 8$, $-21 \le l \le 21$	$-14 \le h \le 14$, $-10 \le k \le 10$, $-26 \le l \le 27$
θ range for data collection (°)	$1.911 \le \theta \le 25.038$	$1.926 \le \theta \le 27.931$
Reflections collected	8140	13,885
Independent/observed reflections	2754/1109	4190/1923
$R_{int.}$	0.0944	0.0816
Refinement method	Full-matrix least-squares on F^2	Full-matrix least-squares on F^2
Data/restraints/ parameters	2754/104/236	4190/170/283
Goodness-of-fit on F^2	0.882	0.901
Final R indices [$I > 2\sigma(I)$]	$R_1 = 0.0569$, $wR_2 = 0.0843$	$R_1 = 0.0542$, $wR_2 = 0.1057$
R indices (all data)	$R_1 = 0.1691$, $wR_2 = 0.1078$	$R_1 = 0.1374$, $wR_2 = 0.1315$
$\Delta\rho_{max.}$, $\Delta\rho_{min.}$ (e/Å^3)	0.40, −0.23	0.38, −0.40

ligands arise from their ability to chelate transition metal ions. The complexation can alter biological properties and lead to new activities that free ligands do not exhibit [41–43]. Nickel metal ions are quite important in biological systems. Nickel is a critical cofactor for many enzymes and metalloenzymes [44]. Therefore, the synthesis of new nickel complexes and their biological activities are attracting attention [21,24,38,45,46]. Especially in recent years, theoretical computational publications have been focused on compounds suitable for biological systems [47–49].

S-alkyl isothiosemicarbazones can also exhibit tetradentate ligand behavior as a result of template reactions. This reaction involves the condensation of the amin group of thioamide with the carbonyl group of an aldehyde or a ketone in the presence of a metal ion [50–54] and these complexes have significant biological applications [55–57].

Herein, two N^1,N^4-disalicylidene-S-alkyl isothiosemicarbazone Ni(II) complexes were prepared using N^1-salicylidene-*S*-methyl-isothiosemicarbazone (**L1**) and N^1-salicylidene-*S*-propylisothiosemi-carbazone (**L2**). The structures of the obtained compounds were characterized through elemental analysis, UV–visible, FT-IR, and ^{1}H NMR spectroscopies. The structures of these complexes (**1** and **2**) were elucidated using XRD and theoretical calculation methods. Additionally, the electronic properties of the complexes, including frontier molecular orbitals, molecular electrostatic potential, charge analysis, and Fukui functions, were determined for the optimized structures using theoretical calculation methods. Topological analyses were performed with Multiwfn to identify the primary binding sites and weak interactions of the complexes. Molecular docking studies were conducted to evaluate the activity of the complexes as potential agents for lung and breast cancer treatment.

2. Material and methods

2.1. Chemicals and apparatus

All chemicals and solvents were of reagent grade and used as received without further purification (methyl iodide, Sigma-Aldrich, ≥99 % purity; n-propyl bromide, Sigma-Aldrich, 99 % purity; thio-semicarbazide, Sigma-Aldrich, 99 % purity; salicylaldehyde, Sigma-Aldrich, 98 % purity; nickel(II) chloride hexahydrate, Sigma-Aldrich, 99.9 % purity; 2-aminopyridine, Sigma-Aldrich, ≥99 % purity; ethanol, Sigma-Aldrich, ≥99.8 % purity; ethanol, Sigma-Aldrich, ≥99.8 % purity). Elemental analyses were performed on a Thermo Finnigan Flash 2000 Elemental Analyzer. IR spectra of the compounds were recorded on a Cary 630 FTIR spectrometer with a diamond ATR from Agilent. ^{1}H nuclear magnetic resonance spectra were recorded on a Varian UNITY INOVA 500 MHz spectrometer using DMSO as solvent. The electronic spectrum was recorded on a Shimadzu UV-2600 UV–Vis spectrophotometer using a pair of matching quartz cuvettes with a thickness of 1 cm.

2.2. Syntheses

2.2.1. Synthesis of the N^1-salicylidene-S-alkylisothiosemicarbazones

The starting materials were prepared using a literature method [52]. Methyl iodide was used for the synthesis of compound **L1** [methyl *N*'-(2-hydroxybenzylidene)carbamohydrazonothioate], while n-propyl bromide was used for the synthesis of compound **L2** [propyl *N*'-(2-hydroxybenzylidene)carbamohydrazonothioate].

Characterization data of the **L1**: The Color: Light Yellow; Yield: 93 %; m.p. (°C): 160; Anal. Calc. For $C_9H_{11}N_3OS$ (209.27 g/mol): C, 51.63; H, 5.32; N, 20.05; S, 15.32; Found: C, 51.66; H, 5.30; N, 20.08; S, 15.28 %. IR (cm^{-1}): 3449 υ(OH); 3278 υ_{sym} (NH_2); 3239 υ_{asym} (NH_2); 1636 δ(N-H); 1615, 1597 υ(C=N); 1145 υ(C-O); 3036, 2967, 2923 υ(C-H). UV–Vis (5.10^{-5} M, $CHCl_3$): ((λ (ε)) 239.5 (41000), 293 (54750), 304.5 (52800), 333.50 (54400). ^{1}H NMR (ppm): 11.60, 10.88 (cis/trans ratio: 2/1, s, 1H, OH), 8.47, 8.35 (syn/anti ratio: 1/2, s, 1H, CH=N^1), 7.55 (m, 1H, *d*),

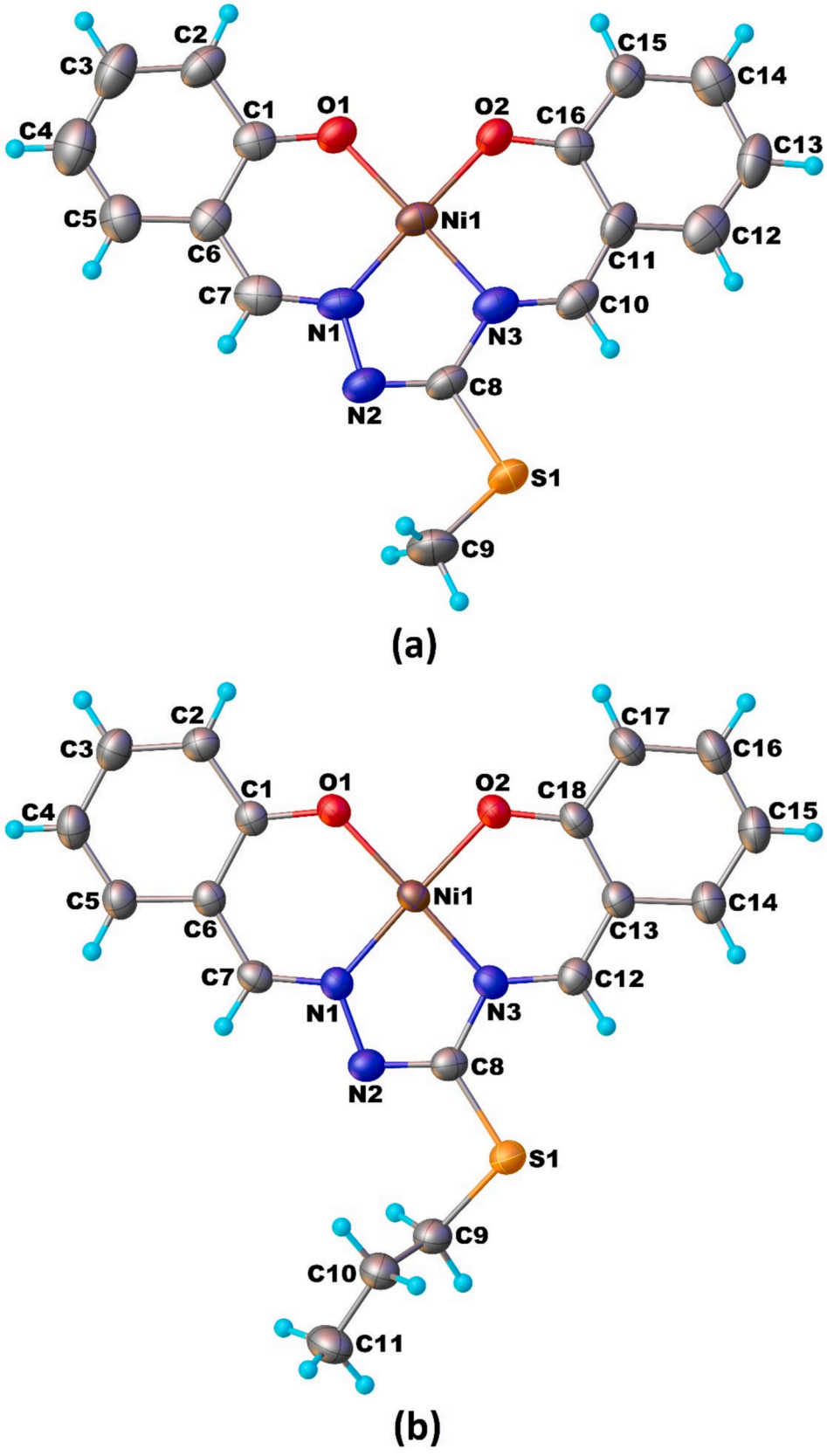

Fig. 1. Molecular structures of **1** (a) and **2** (b) showing the atom-labelling scheme. Displacement ellipsoids are drawn at the 20% probability level and H atoms are shown as small spheres of arbitrary radii. For simplicity, only the major parts of the disordered fragments are shown.

Table 2
Selected bond lengths (Å) and angles (°) for **1** and **2**.

Parameters	1		Parameters	2	
	X-ray	DFT		X-ray	DFT
Bond lengths					
Ni1—O1	1.818(4)	1.840	Ni1—O1	1.845(3)	1.839
Ni1—O2	1.831(5)	1.850	Ni1—O2	1.842(3)	1.850
Ni1—N1	1.835(6)	1.839	Ni1—N1	1.837(3)	1.839
Ni1—N3	1.837(5)	1.858	Ni1—N3	1.825(3)	1.858
S1—C8	1.779(10) [1.679 (17)]	1.761	S1—C8	1.737(6) [1.731(7)]	1.762
S1—C9	1.706(7) [1.647(9)]	1.809	S1—C9	1.779(6) [1.781(7)]	1.823
O1—C1	1.298(8)	1.292	O1—C1	1.309(5)	1.291
O2—C16	1.261(7)	1.282	O2—C18	1.306(5)	1.282
N1—N2	1.349(9) [1.280 (16)]	1.372	N1—N2	1.373(5) [1.358(6)]	1.372
N1—C7	1.294(8)	1.308	N1—C7	1.297(5)	1.308
N2—C8	1.296(10) [1.323 (16)]	1.294	N2—C8	1.302(6) [1.308(6)]	1.294
N3—C8	1.490(13) [1.490 (16)]	1.391	N3—C8	1.450(6) [1.448(7)]	1.391
N3—C10	1.297(8)	1.318	N3—C12	1.328(5)	1.318
Bond angles					
O1—Ni1—O2	85.9(2)	87.23	O1—Ni1—O2	86.49(13)	87.18
O1—Ni1—N1	95.5(2)	94.92	O1—Ni1—N1	95.83(13)	94.91
O1—Ni1—N3	178.2(3)	178.04	O1—Ni1—N3	178.90 (13)	178.03
O2—Ni1—N1	177.8(2)	177.85	O2—Ni1—N1	177.33 (14)	177.91
O2—Ni1—N3	95.4(2)	94.72	O2—Ni1—N3	94.61(14)	94.80
N1—Ni1—N3	83.2(3)	83.12	N1—Ni1—N3	83.07(15)	83.11
C8—S1—C9	102.5(5) [113.9(8)]	100.07	C8—S1—C9	103.7(3) [103.6(4)]	101.07
N2—C8—S1	119.8(10) [110.9 (15)]	120.66	N2—C8—S1	121.2(5) [118.8(6)]	121.15
N3—C8—S1	116.1(8) [122.7 (12)]	120.36	N3—C8—S1	120.9(4) [122.4(5)]	120.08
N2—N1—C7	111.1(7) [107.0(8)]	115.98	N2—N1—C7	114.8(4) [112.7(4)]	116.02
N1—N2—C8	103.0(9) [100.3 (15)]	110.68	N1—N2—C8	109.1(5) [108.9(6)]	110.83
N1—C7—C6	127.3(8)	124.28	N1—C7—C6	125.2(4)	124.30
N2—C8—N3	124.1(10) [126.5 (16)]	118.98	N2—C8—N3	117.8(5) [118.0(6)]	118.77
C8—N3—C10	127.4(7) [131.3(9)]	122.58	C8—N3—C12	120.8(4) [123.3(4)]	122.57
N3—C10—C11	124.2(7)	124.70	N3—C12—C13	123.4(4)	124.73

Note: Parameters for the minor parts of the disordered fragments are quoted in square brackets.

7.39 (dt, 1H, *b*), 7.25 (m, 1H, *c*), 6.93 (s, wide, 2H, NH_2), 6.89 (m, 1H, *a*), 2.45, 2.39 (cis/trans ratio: 2/1, s, 3H, S–CH_3).

Characterization data of the **L2**: The Color: Yellow; Yield: 91 %; m.p. (°C): 188; Anal. Calc. For $C_{11}H_{15}N_3OS$ (237.32 g/mol): C, 55.67; H, 6.37; N, 17.71; S, 13.51; Found: C, 55.66; H, 6.39; N, 17.75; S, 13.48 %. IR (cm^{-1}): 3434 υ(OH); 3300 $υ_{sym}$ (NH_2); 3266 $υ_{asym}$ (NH_2); 1641 δ(N-H); 1616, 1597 υ(C=N); 1149 υ(C-O); 3015, 2948, 2915 υ(C-H). UV–Vis (5.10^{-5} M, $CHCl_3$): ((λ (ε)) 239.5 (35750), 293.5 (21580), 304.5 (51850), 334 (54000). ^{1}H NMR (ppm): 11.70, 10.87 (cis/trans ratio: 2/1, s, 1H, OH), 8.40, 8.37 (syn/anti ratio: 2/3, s, 1H, CH=N^1), 7.56 (d, 1H, *d*), 7.39 (d, 1H, *b*), 7.24 (dd, 1H, *c*), 6.94 (d, 2H, NH_2), 6.89 (t, 1H, *a*), 2.97 (dd, 2H, $^1CH_2$), 1.64 (m, 2H, $^2CH_2$), 0.98 (m, 3H, $^3CH_3$).

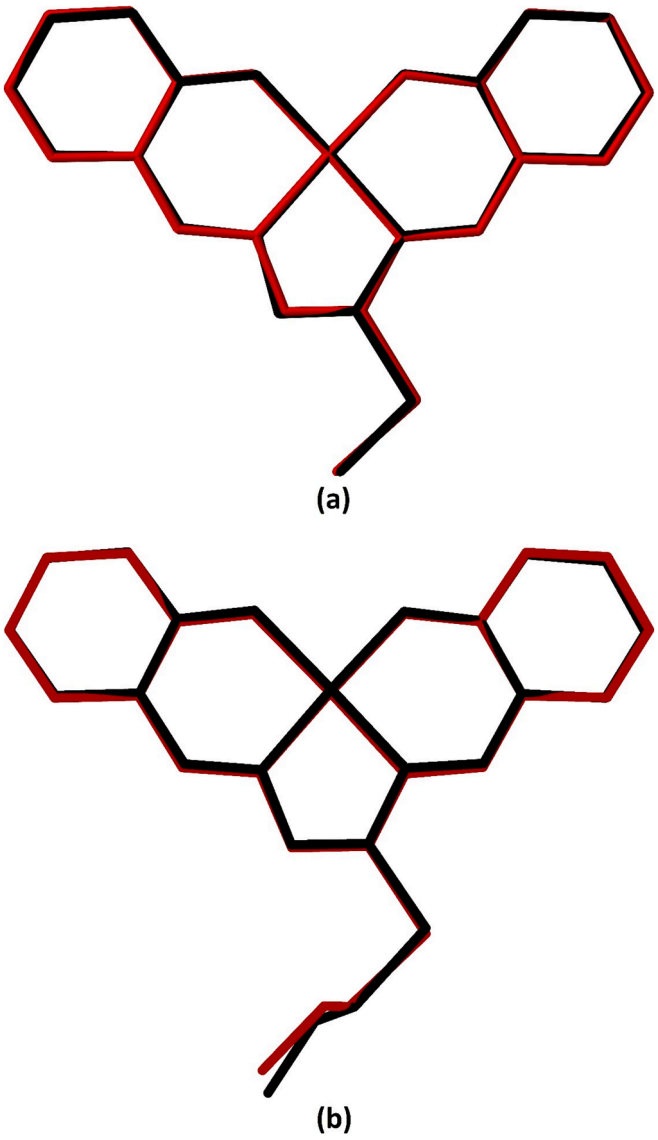

Fig. 2. Atom-by-atom superimposition of the structures calculated (red) over the X-ray structure (black) for **1** (a) and **2** (b). H atoms were not taken into account in the determination of RMSD values.

2.2.2. Synthesis of the N^1,N^4-disalicylidene-S-alkyl isothiosemicarbazone Ni(II) chelates

For the synthesis of complex **1** {[methyl *N,N'*-bis{[2-(hydroxy) phenyl]methylidene}carbamohydrazonothioatato]-nickel}, the starting material **L1** (0.2 g, 1 mmol) was dissolved in methanol and added to a solution of $NiCl_2{\cdot}6H_2O$ (0.24 g, 1 mmol) in methanol (10 mL). The mixture was stirred at 60 °C for 5 min. Subsequently, 2-aminopyridine (0.095 g, 1 mmol) was added, and the reaction was allowed to proceed for 1 h. After approximately 2 weeks, red crystals were isolated. (Scheme 1). Complex **2** {[propyl *N,N'*-bis{[2-(hydroxy)phenyl]methylidene}carbamohydrazonothioatato]-nickel} was synthesized in the same way by using **L2** instead of **L1**, in the same stoichiometric ratio. Both products were isolated in a dark red crystalline form soluble in alcohol and chloroform and very much soluble in polar aprotic solvents such as DMF and DMSO.

Characterization data of the complex **1**: The Color: Dark Red; Yield: 62 %; m.p. (°C): 223; Anal. Calc. For $C_{16}H_{13}N_3OSNi$ (370.05 g/mol): C, 51.93; H, 3.54; N, 11.36; S, 8.66; Found: C, 51.96; H, 3.58; N, 11.37; S, 8.61 %. IR (cm^{-1}): 1604, 1589, 1577 υ(C=N); 1154 υ(C-O); 3052, 3004, 2919 υ(C-H). UV–Vis (5.10^{-5} M, $CHCl_3$): ((λ (ε)) 240 (54500), 301

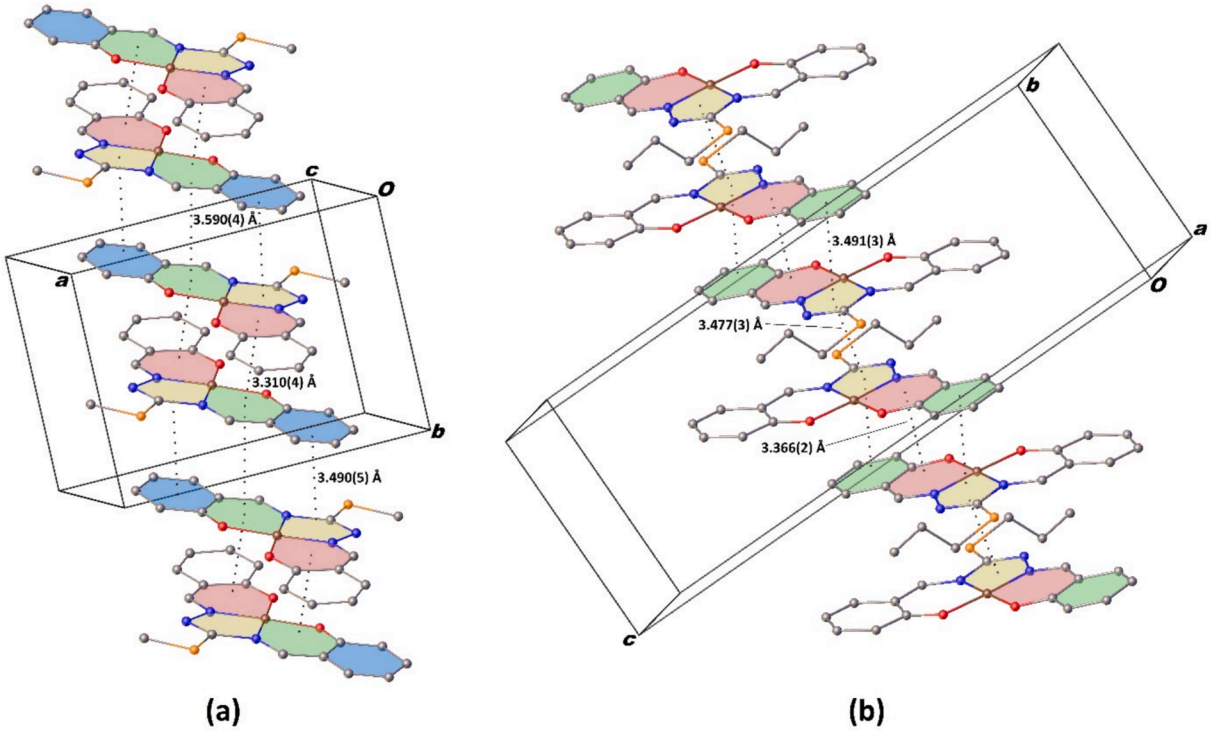

Fig. 3. Crystal structure of **1** (a) and **2** (b) showing the formation of a π-stacked chain along [010]. For the sake of clarity, the H atoms have all been omitted.

(25200), 323.5 (18500), 397.50 (21400), 471.5 (8190), 552 (5000). ^{1}H NMR (ppm): 8.55 (s, 1H, CH=N^1), 8.32 (s, 1H, CH=N^4), 7.78 (dd, 1H, *d*), 7.57 (dd, 1H, *h*), 7.48 (ddd, 1H, *b*), 7.32 (ddd, 1H, *f*), 6.99 (m, 1H, *c*), 6.94 (m, 1H, *g*), 6.74 (ddd, 1H, *a*), 6.68 (ddd, 1H, *e*), 2,74 (s, 3H, S–CH_3).

Characterization data of the complex **2**: The Color: Dark Red; Yield: 44 %; m.p. (°C): 236; Anal. Calc. For $C_{18}H_{17}N_3OSNi$ (398.11 g/mol): C, 54.30; H, 4.30; N, 10.56; S, 8.06; Found: C, 54.36; H, 4.28; N, 10.57; S, 8.02 %. IR (cm^{-1}): 1603, 1590, 1577 υ(C=N); 1143 υ(C-O); 3055, 3014, 2969 υ(C-H). UV–Vis (5.10^{-5} M, $CHCl_3$): ((λ (ε)) 239.5 (46500), 301.5 (20000), 325.5 (14500), 397 (17000), 471.5 (7500), 552 (4000). ^{1}H NMR (ppm): 8.56 (s, 1H, CH=N^1), 8.38 (s, 1H, CH=N^4), 7.79 (dd, 1H, *d*), 7.59 (dd, 1H, *h*), 7.49 (ddd, 1H, *b*), 7.33 (ddd, 1H, *f*), 7.00 (d, 1H, *c*), 6.94 (d, 1H, *g*), 6.75 (t, 1H, *a*), 6.69 (t, 1H, *e*), 2.29 (t, 2H, CH_2), 1.78 (m, 2H, CH_2) 0.86 (t, 3H, CH_3).

2.3. X-ray crystallography

X-ray diffraction data were recorded with an STOE IPDS II diffractometer at room temperature using graphite-monochromated Mo Kα radiation by applying the ω-scan method. Data collection and cell refinement were carried out using X-AREA [58], while data reduction was performed using X-RED32 [58]. The structures were solved by a dual-space algorithm using SHELXT [59] and refined using full-matrix least-squares calculations on F^2 using SHELXL [60]. All H atoms were placed in idealized positions and treated using a riding model, fixing the bond lengths at 0.93, 0.97, and 0.96 Å for CH, CH_2, and CH_3 atoms, respectively. The displacement parameters of the H atoms were included as $U_{iso}(H) = 1.2U_{eq}$ ($1.5U_{eq}$ for CH_3). Atoms S1/N2/C8/C9 in complex **1** and atoms S1/N2/C8/C9/C10/C11 in complex **2** were disordered over two positions and the refined site-occupancy factors of the disordered atom are 0.719(4)/0.281(4)% for complex **1** and 0.842(2)/0.158(2)% for complex **2**. Crystal data, data collection, and structure refinement details are collected in Table 1. Molecular graphics were generated using OLEX2 [61].

2.4. Computational methods

Computer-based calculations for the initial structures obtained from XRD data for complexes **1** and **2** were performed using the Gaussian 09 W package program [62,63]. Also, the Gauss View 5.0 program was used for visualizations [64]. Optimization, frequency, and electronic property calculations were carried out with the DFT/HSEH1PBE method, using the cc-pvdz (for C, H, N, O, and S atoms) and LanL2DZ (for Ni atom) basis sets together [65,66]. This level of theory was chosen since diverse studies have reported that it yields theoretical results in good agreement with the experimental values in general [67–70]. ^{1}H NMR chemical shift values were calculated using the cc-pvdz and LanL2DZ basis sets together [71]. UV–Vis spectrum analyses were performed with the same basis sets in the TD-DFT/HSEH1PBE method and IEFPCM model in chloroform solvent [72]. Images for ELF, LOL, and dual descriptor analyses were created using the Multiwfn program. Topological analyses of base pairs at different orientations were conducted utilizing the Multiwfn and VMD software applications [73].

2.5. Molecular docking

Molecular docking studies were performed with the Auto dock 4.2.6 Tools program [74]. These selected proteins for the key targets, such as HepG-2 (PDB ID:2OH4) and MCF-7 (PDB ID:3W2S), have been deposited in the RCSB Protein Data Bank [75]. Hence, we needed to perform the SiteMap analysis for the selection of suitable binding or active sites for the proteins of interest. The binding site was selected for the HepG-2, which includes residues His814, Leu838, Gly839, Val846, Ala864, Lys866, Leu880, Glu883, Ile886, Ile887, His889, Ile890, Val896, Val897, Val912, Val914, Glu915, Phe916, Cys917, Gly920, Asn921, Leu1017, Arg1020, Lys1021, Cys1022, Ile1023, His1024, Arg1025, Leu1033, Lys1041, Ile1042, Cys1043, Asp1044, Phe1045, Gly1046, Leu1047, Arg1049 of chain A. In the same way, the active sites were selected for MCF-7, which include residues Leu718, Gly719, Ser720, Gly721, Ala722, Phe723, Gly724, Val726, Ala743, Lys745, Leu747, Arg748, Glu749, Ala750, Thr751, Met766, Cys775, Arg776, Leu777,

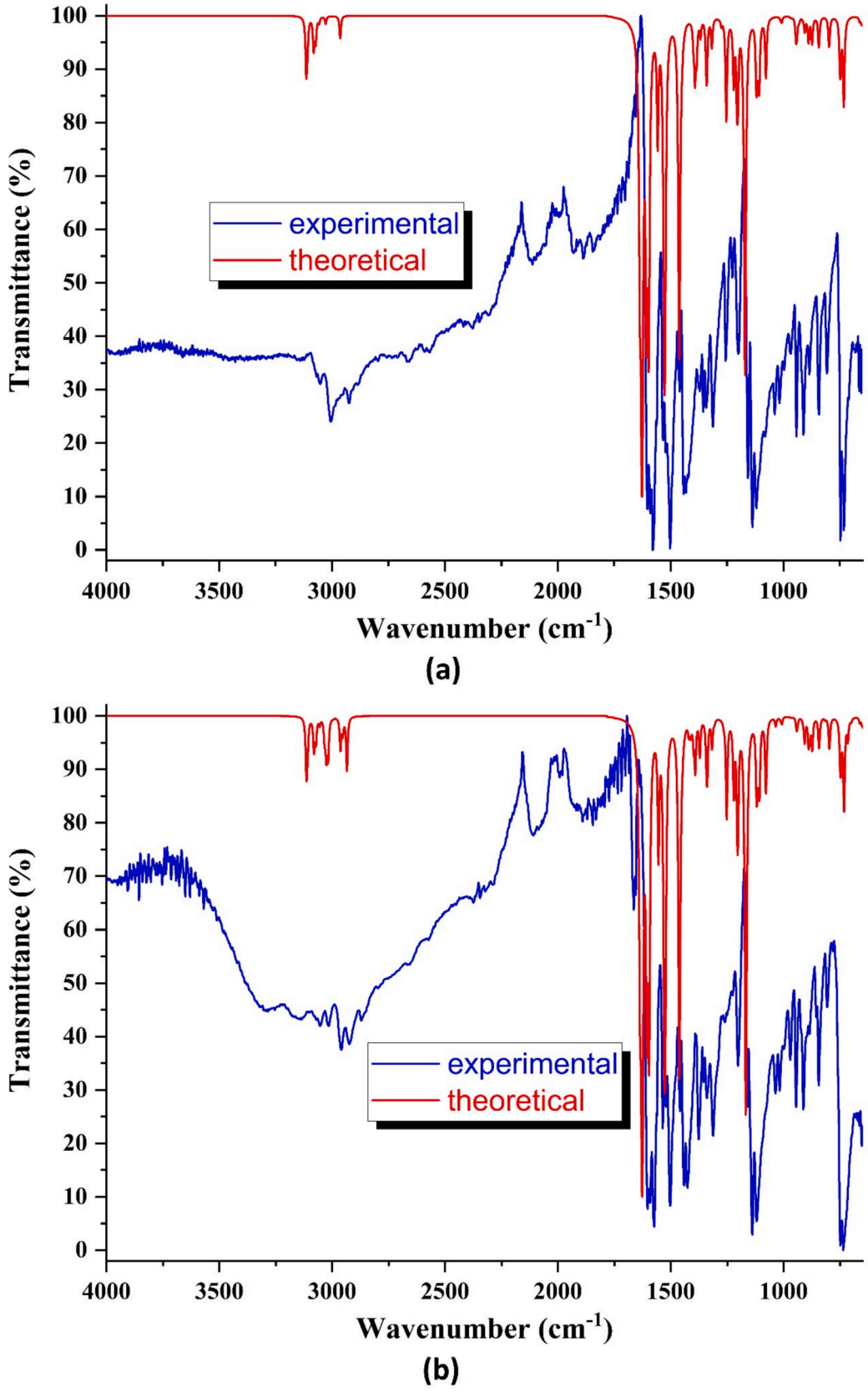

Fig. 4. Experimental and theoretical FT-IR spectra of the **1** (a) and **2** (b).

Table 3
Experimental and calculated frequency values with mode assignments of **1**.

	Calculated		Observed		
Mode	Fre	Fre[a]	I_{IR}[b]	IR	TED
36	680	653	0.50	654 m	$12\delta_{NiNN}+ + 21\delta_{CCN} + 28\delta_{CCC}$
37	688	662	0.39	665 m	$13\upsilon_{NiO} + 11\upsilon_{NiN} + 32\delta_{CCO}$
39/40	761/762	731/732	8.24	732 vs	$69\Gamma_{CCCH}$
41/42	776/779	746/749	3.46	749 vs	$21\Gamma_{CCCH} + 10\Gamma_{CCCC}+ + 38\Gamma_{CCCO}$
46	878	843	1.92	844 s	$65\Gamma_{CCCH} + 21\Gamma_{CCCO}$
48	924	888	2.23	886 m	$15\delta_{CCH} + 28\Gamma_{CCCH}$
51	953	916	0.08	913 s	$77\Gamma_{CCCH}$
53/54	977/980	939/942	1.17	942 s	$78\Gamma_{CCCH}$
56/57	1001/1007	962/968	0.08	967 m	$70\Gamma_{CCCH}$
58/59	1047/1053	1007/1012	0.50	1018 s	$47\upsilon_{CC} + 24\delta_{CCH}$
61/62	1151/1155	1106/1110	4.85	1083 m	$78\Gamma_{CCCH}$
63/64	1163/1165	1117/1120	3.99	1120 vs	$72\delta_{CCH}$
65	1217	1169	51.18	1160 s	$26\upsilon_{CN} + 10\delta_{CCH}$
66/67	1250/1254	1201/1205	5.98	1201 s	$12\delta_{HCH} + 27\delta_{CCH} + 24\Gamma_{CCCH}$
68	1269	1220	5.77	1228 m	$21\upsilon_{NN} + 29\delta_{CCH}$
69	1303	1252	9.84	1258 m	$10\upsilon_{CC} + 17\delta_{CCH}$
71	1369	1316	2.59	1314 s	$19\upsilon_{CO} + 34\delta_{CCH}$
72/73/74	1393/1398/1395	1338/1340/1344	3.62	1341 s	$11\upsilon_{CC} + 42\delta_{CCH}$
75	1422	1367	1.55	1369 s	$73\delta_{HCH} + 26\Gamma_{HCSC}$
79	1497	1439	0.20	1435 s	$30\upsilon_{CC} + 12\delta_{CCC} + 10\delta_{CCH}$
80	1506	1447	0.92	1446 s	$10\upsilon_{CC} + 32\delta_{CCH}$
82	1520	1460	46.89	1459 m	$25\upsilon_{CC} + 28\delta_{CCH}$
83/84	1585/1589	1523/1527	35.98	1536 s	$33\upsilon_{CC} + 11\delta_{CCC} + 14\delta_{CCH}$
85	1619	1556	11.27	1577 vs	$12\upsilon_{CN} + 52\upsilon_{CC}$ (C=N)
86	1660	1595	43.45	1589 s	$10\upsilon_{CN} + 52\upsilon_{CC} + 12\delta_{CCH}$(C=N)
87	1671	1605	37.41	1604 vs	$12\upsilon_{CN} + 58\upsilon_{CC}$ (C=N)
90	3081	2961	1.98	2919 vw	$99\upsilon_{CH}$(sym, CH3)
91	3148	3025	0.68	3004 vw	$100\upsilon_{CH}$ (asy, ring)
92	3178	3054	0.52	3052vw	$100\upsilon_{CH}$ (asy, ring)

υ: stretching, δ: in-plane bending, γ: out-of bending Γ: torsion, s: strong, m: medium, w: weak, v: very.
[c]Total energy distribution level (TED) less than 10% are not shown.
[a] 0.961 was used as the scaling factor for all wavenumbers calculated at DFT/HSEH1PBE/cc-pvdz + LanL2DZ [71].
[b] Relative absorption intensities normalized with highest peak absorption equal to 100.

Val786, Ile788, Ile789, Thr790, Gln791, Leu792, Met793, Phe795, Gly796, Cys797, Leu799, Asp800, Arg803, Glu804, His805, His835, Arg836, Asp837, Ala839, Arg841, Asn842, Leu844, Thr854, Asp855, Phe856, Gly857, Leu858, Ala859, Leu862, Lys875, Val876, Pro877, Ile878,Lys879, Trp880, Met881, Thr891, Glu906, Ser912, Lys913, Ala920. The nickel complexes in the output format from the Gaussian 09 program have been converted into docking format (.pdbqt) by using Open Babel, and the genetic algorithm (GA) parameters were tethered to the protein using 10 runs of the GA criteria. Then, non-polar hydrogen was added, and the AD4 parameters for nickel were set, while all other settings remained default. Visualizations for docking poses were created using the Discovery Studio Visualizer program [76].

Table 4
Experimental and calculated frequency values with mode assignments of **2**.

	Calculated		Observed		
Mode	Fre	Fre[a]	I_{IR}[b]	IR	TED
40	679	652	0.50	654 vw	$13\delta_{NiNN} + 24\delta_{CCN}$
41	689	662	0.47	665 vw	$12\upsilon_{NiO} + 10\upsilon_{NiN} + 28\delta_{CCO}$
44/45	761	732	8.54	736 vs	$72\Gamma_{CCCH}$
46/47	775/779	745/749	3.42	751 vs	$33\Gamma_{CCCH} + 38\Gamma_{CCCO}$
51/52	875/877	841/843	1.97	846 s	$31\Gamma_{CCCH} + 38\Gamma_{CCCO}$
59/60	975/980	937/942	1.09	944 s	$78\Gamma_{CCCH}$
61/62	1000/1007	961/968	0.07	970 m	$73\Gamma_{CCCH}$
63/67	1047/1053	1006/1012	0.57	1017 s	$44\upsilon_{CC} + 14\delta_{CCH}$
65/66	1069/1076	1028/1034	0.75	1037 s	$41\delta_{HCS} + 26\Gamma_{CCCH}$
71/72	1162/1165	1117/1119	4.74	1120 vs	$64\delta_{CCH}$
73	1214	1166	6283	1163 s	$39\upsilon_{CN} +19\delta_{CCH}$ tek CN
75/76	1250/1252	1201/1204	8.01	1202 m	$13\delta_{HCH} + 33\delta_{CCH} + 26\Gamma_{CCCH}$
78	1269	1220	6.68	1225 m	$15\upsilon_{NN} + 24\delta_{CCH}$
82	1370	1316	2.60	1314 s	$18\upsilon_{CO} + 33\delta_{CCH}$
84/85	1394/1395	1337/1338	3.62	1341 m	$13\upsilon_{CC} + 35\delta_{CCH}$
86	1398	1343	2.62	1354 m	$18\upsilon_{CC} + 23\delta_{CCH}$
87	1425	1370	3.35	1376 s	$64\delta_{HCH} + 13\Gamma_{HCSC}$
92	1476	1419	1.10	1423 s	$74\delta_{HCH}$
93	1497	1439	0.21	1440 vs	$27\upsilon_{CC} + 12\delta_{CCC} + 25\delta_{CCH}$
96	1520	1460	51.62	1461 s	$21\upsilon_{CC} + 12\delta_{CCC} + 28\delta_{CCH}$
97/98	1585/1589	1523/1527	36.81	1524 s	$24\upsilon_{CC} + 17\delta_{CCH}$
99	1619	1553	12.79	1577 vs	$15\upsilon_{CN} +52\upsilon_{CC}$ (C=N)
100	1659	1595	45.03	1589 vs	$12\upsilon_{CN} +54\upsilon_{CC}$ (C=N)
101	1670	1605	37.16	1604 vs	$11\upsilon_{CN} +58\upsilon_{CC}$ (C=N)
102/103	1691/1701	1625/1634	100	1663 m	$54\upsilon_{CC}$
104	3051	2932	4.87	2969 vw	$94\upsilon_{CH}$ (sym, CH3)
108	3137	3015	3.49	3014 vw	$87\upsilon_{CH}$ (asy, CH_2, CH_3)
112	3176	3052	0.59	3055 vw	$99\upsilon_{CH}$ (asy, ring)

υ: stretching, δ: in-plane bending,γ: out-of bending Γ: torsion, s: strong, m: medium, w: weak, v: very.
[c]Total energy distribution level (TED) less than 10% are not shown.
[a] 0.961 was used as the scaling factor for all wavenumbers calculated at DFT/HSEH1PBE/cc-pvdz + LanL2DZ [71].
[b] Relative absorption intensities and relative Raman intensities normalized with highest peak absorption equal to 100.

3. Results and discussion

3.1. Experimental and theoretical structures

The solid-state structures of **1** and **2** have been unambiguously determined by single crystal X-ray analysis. Perspective views of the complexes are presented in Fig. 1, while relevant bond lengths and angles are documented in Table 2.

The complexes are formed by chelating a thiosemicarbazone ligand to a Ni(II) metal center. The Schiff-base ligands undergo double deprotonation to act as an *O,N,N,O* tetradentate ligand, coordinating *via* its two phenolate oxygen atoms (O1 and O2) and two azomethine nitrogen atoms (N1 and N3). The difference in the composition of the two molecules originates from the thiosemicarbazone ligands, propyl versus methyl groups on the S atom. The central nickel atoms lie in a four-coordinate environment and adopt a slightly distorted square-planar geometry. Coordination of the symmetric $[N_2O_2]$ donors to the nickel atoms generates three approximately planar chelate rings, two six-

Table 5
Experimental and theoretical ^{1}H NMR chemical shift values of **1** and **2**.

	1			2	
ATOMS	Experimental	Theoretical	ATOMS	Experimental	Theoretical
H2	6.74	7.67	H2	6.75	7.69
H3	7.48	7.98	H3	7.49	7.98
H4	6.99	7.29	H4	7.00	7.29
H5	7.78	7.91	H5	7.79	7.93
H7	8.55	9.23	H7	8.56	9.23
H10	8.32	8.96	H12	8.38	9.01
H12	7.57	7.99	H14	7.59	7.98
H13	6.94	7.34	H15	6.94	7.34
H14	7.32	8.11	H16	7.33	8.11
H15	6.68	7.72	H17	6.69	7.72
H16	2.74	3.23	H18	2.29	3.95
H17	2.74	3.23	H19	2.29	3.27
H18	2.74	2.90	H20	1.78	2.51
			H21	1.78	2.01
			H22	0.86	1.51
			H23	0.86	1.78
			H24	0.86	1.51

membered ($NiONC_3$) and one five-membered (NiN_3C). The Ni—N bond distances are 1.835(6) and 1.837(5) Å for **1**, and 1.837(3) and 1.825(3) Å for **2**. The Ni—O bond distances are 1.818(4) and 1.831(5) Å for **1** and 1.845(3) and 1.842(3) Å for **2**. The Ni—N and Ni—O bonds are found in the range of 1.839–1.850 Å and 1.839–1.858 Å for the optimized structures, respectively. These coordination bond distances are comparable to those found in similar Ni(II)-salen-type complexes [77–82].

As can be seen from the *trans* angles, which vary from 177.33(14)° to 178.90(13)°, and the *cis* angles, which change from 83.07(15)° to 95.83 (13)°, the coordination around the Ni(II) ions is distorted. These angles span ranges of 177.85°-178.04° and 83.11°-94.92°, respectively, in the calculated structures. For quantitative evaluation of the extent of distortion around the metal centers, the four-coordinate structural indexes τ_4 [83] and τ_4' [84] were employed;

$$\tau_4 = \frac{360^\circ - (\alpha+\beta)}{360^\circ - 2\theta}\tau_4' = \frac{\beta-\alpha}{360^\circ-\theta} + \frac{180^\circ-\beta}{180^\circ-\theta} \quad (1)$$

where α and β ($\beta > \alpha$) are the two largest valence angles and θ is the ideal tetrahedral angle (109.5°). The τ_4 and τ_4' values are 0 for an ideal square-planar geometry while these become 1 for an ideal tetrahedral coordination sphere. The values of the calculated τ_4 and τ_4' geometry indices are both 0.03 for **1**, and 0.03 and 0.02 for **2**, respectively. Both indices were calculated to be 0.03 for the DFT structures.

The most common way to see the three-dimensional similarity of the X-ray and DFT structures is to superimpose them. As a result of this process, the root mean square deviation (RMSD) values were obtained 0.103 and 0.203 Å for 1 and 2, respectively (Fig. 2). These values show that the agreement between the two structures is good, and the level of theory can be used in the calculation of electronic properties. The reason for the observed difference between theoretical and experimental data is that the theoretical calculations are performed for a single molecule isolated in an environment where there is no Coulombic interaction. Because the molecule in the crystal lattice is in Coulombic interaction [85].

There are no intramolecular interactions in the molecular structures of the complexes. In their crystal structures, no classic hydrogen bonds are found. Instead, the molecules are linked into centrosymmetric dimers by $\pi\cdots\pi$ stacking interactions. The Ni···Ni separation in the centrosymmetric dimer is 3.266 Å in **1** and 4.190 Å in **2**, suggesting the absence of Ni—Ni bonding interactions [86]. In **1**, the two different six-membered chelate rings in the molecules at (x, y, z) and (1–x, 1–y, 1–z) are mutually parallel with a distance of 3.310(4) Å between the ring centroids. Further, $\pi\cdots\pi$ stacking interactions between the five-membered chelate ring and (C11-C16) benzene ring and between the (Ni1/O2/N3/C10/C11/C16) chelate rings in the molecules at (x, y, z) and (1–x, 2–y, 1–z) are also observed, with a distance of 3.490(5) and 3.590(4) Å between the ring centroids, respectively. In **2**, the five-membered chelate ring in the molecule at (x, y, z) stacks above its symmetry-related partner at (1–x, 1–y, 1–z), with a distance of 3.477(3) Å between the ring centroids. In addition, $\pi\cdots\pi$ stacking interactions between the five-membered chelate ring and (C1-C6) benzene ring and between the (Ni1/O1/N1/C1/C6/C7) chelate rings in the molecules at (x, y, z) and (1–x, 2–y, 1–z) exist, the corresponding ring-centroid separations being 3.491(3) and 3.366(2) Å, respectively. Propagation by translation and inversion of these interactions then leads to the formation of a π-stacked chain of centrosymmetric molecules running parallel to the [010] direction (Fig. 3).

3.2. Vibrational analysis

The recorded FT-IR spectra of the synthesized complexes are shown in Fig. 4. Tables 3 and 4 present the experimental frequency values and the theoretical frequency values generated by the calculation methods corresponding to these values along with mode assignments for complex **1** and complex **2**, respectively. Mode assignments were performed with the Veda program [87]. Theoretical frequency values were scaled by a scale factor of 0.961 to ensure consistency between experimental and theoretical values [88].

The IR spectral analysis of the ligands revealed bands at approximately 3460 cm^{-1} for υ(OH) stretching vibrations, 3280 cm^{-1} and 3230 cm^{-1} for symmetric and asymmetric $\upsilon(NH_2)$ stretching, around 1630 cm^{-1} for δ(N–H) in-plane bending, and at 1610 cm^{-1} and 1590 cm^{-1} for υ(C=N) stretching vibrations. After chelation, the bands corresponding to the amino and hydroxyl groups were observed, alongside the emergence of three distinct bands attributed to the vibrations of the C=N groups.

For **1**, the C–H stretching vibrations were observed at 3052 (vw), 3004 (vw), and 2919 (vw) cm^{-1} in the experimental spectrum while they were theoretically calculated at 3054, 3025, and 2961 cm^{-1}. Also, these stretching vibrations were observed at 3055 (vw), 3014 (vw), and 2969 (vw) cm^{-1} in the experimental spectrum of **2**, and they were calculated at 3052, 3015, and 2932 cm^{-1}. The C–H stretching vibrations recorded and calculated for the title complexes were obtained in the region of 2800–3100 cm^{-1}, which is given in the literature for this stretching vibration of heteroaromatic structures [89].

The C–C stretching vibrations for the aromatic rings of heterocyclic compounds are often detected in the range of 1650–1200 cm^{-1} [90]. The C–C stretching vibration values for **1** were observed at 1536 (s), 1459 (m), 1446 (s), 1435 (s), 1341 (s), and 1258 (m) cm^{-1} and calculated at 1523/1527, 1466, 1447, 1338/1340/1344, and 1252 cm^{-1}.

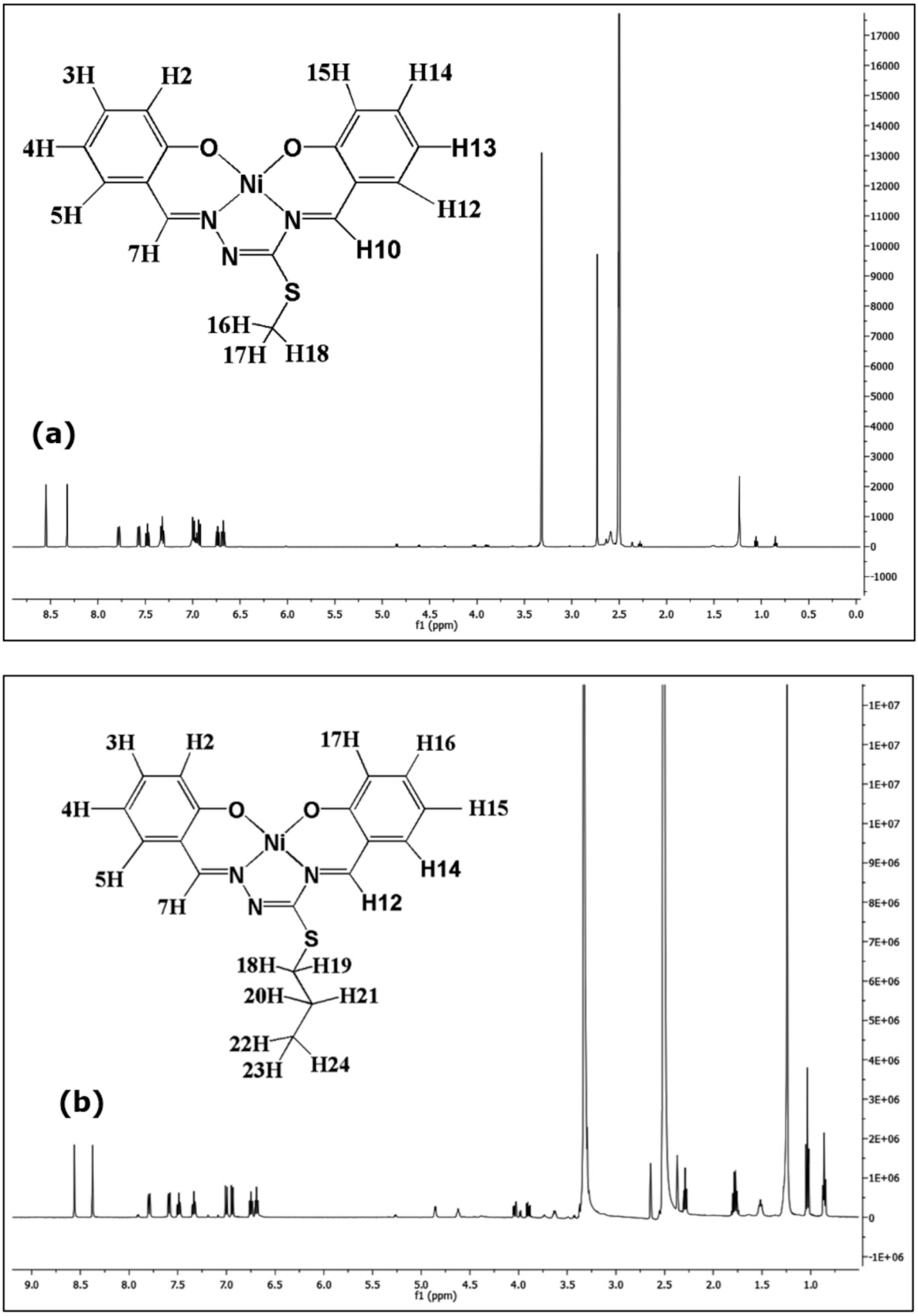

Fig. 5. Experimental ^{1}H NMR spectra **1** (a) and **2** (b).

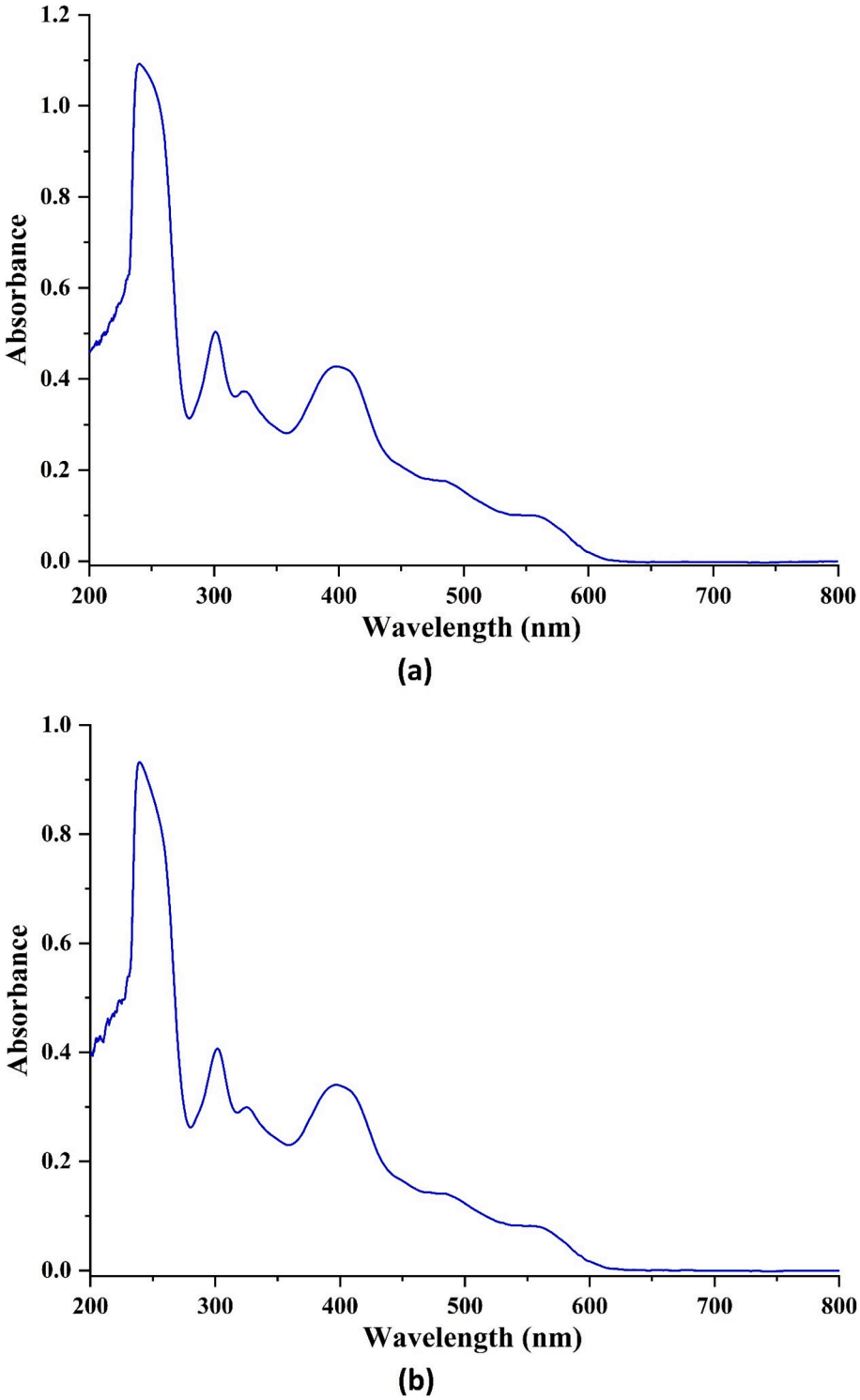

Fig. 6. Experimental UV–Vis spectra of the **1** (a) and **2** (b).

These vibration values of **2** were assigned at 1663 (m), 1524 (s), 1461 (s), 144 (vs), 1354 (m), and 1341 (m) cm^{-1}. Also, theoretical values were calculated at 1625/1634, 1523/1527, 1460, 1439, 1343, and 1337/1338 cm^{-1}.

The C=N stretching vibrations for **1** and **2** were observed at 1604 (vs), 1589 (s), and 1577 (vs) cm^{-1} in the FT-IR spectrum, and the theoretical values of these vibrations were calculated at 1605, 1595, and 1556 cm^{-1}. For the two complexes, both C=N stretching vibrations were observed within the appropriate ranges given in the literature [91,92].

The C-O stretching vibration was observed at 1154 and 1143 cm^{-1} in the IR spectra of 1 and 2, but no corresponding values could be obtained in the calculations made for both complexes. Also, this stretching vibration occurred at 1314 cm^{-1} for **1** and **2** in the IR spectra and was calculated at 1316 cm^{-1}. In another study, two new square-planar nickel (II) complexes were synthesized from (2-((E)-(9-ethyl-9H-carbazole-7-ylimino)methyl)phenol) (SIC) and (1-((E)-(9-ethyl-9H-carbazole-7-ylimino)methyl)naphthalene-2-ol) (NIC) ligands, and their spectroscopic characterization was carried out. In this study, C-O stretching vibrations

Table 6
Experimental and theoretical UV–Vis. parameters of the **1** and **2**.

Molecule	Experimental	Theoretical				
	λ (nm)	λ (nm)	E (eV)	f	Symmetry	Major Contributions
1	552	502	2.47	0.0951	Singlet-A	HOMO → LUMO %97
	471.5	429	2.88	0.1435	Singlet-A	HOMO-1 → LUMO %91
	397.5	–	–	–	–	–
	323.5	–	–	–	–	–
	301	–	–	–	–	–
	240	–	–	–	–	–
2	552	502	2.47	0.0976	Singlet-A	HOMO → LUMO %97
	471.5	429	2.88	0.1466	Singlet-A	HOMO-1 → LUMO 91 %
	397	–	–	–	–	–
	325.5	–	–	–	–	–
	301.5	–	–	–	–	–
	239.5	–	–	–	–	–

Table 7
Energy values of HOMO-LUMO molecular orbitals of **1** and **2**, as well as other quantum chemical properties.

Parameters	Energy Values (eV)	
	1	2
E_{HOMO}	−5.33	−3.24
E_{LUMO}	−2.81	−0.70
Energy band gap ($\Delta E = E_{LUMO} - E_{HOMO}$)	2.52	2.54
Iozination potential ($I = -E_{LUMO}$)	5.33	3.24
Electron affinity ($A = -E_{HOMO}$)	2.81	0.70
Chemical hardness ($\eta = -(E_{HOMO} + E_{LUMO})/2$)	1.26	1.27
Chemical softness ($\sigma = 1/2\eta$)	0.80	0.79
Electronegativity ($\chi = \mu_c$)	4.07	1.97
Chemical potential ($\mu_c = (E_{HOMO} - E_{LUMO})/2$)	−4.07	−1.97
Global electrophilicity ($\omega = \mu_c^2/2\eta$)	6.60	1.52

of the synthesized complexes were observed at 1335 and 1399 cm^{-1}, respectively [93].

The N-N stretching vibrations of the title complexes were assigned at 1225 and 1228 cm^{-1} for complex **1** and complex **2**, respectively, and calculated at 1220 cm^{-1}. The Ni-O and Ni-N stretching vibrations resulting from the coordination of nitrogen and oxygen atoms to nickel atoms were assigned at 665 (vw) cm^{-1} in both complexes. According to theoretical calculations, the value for this mode is 662 cm^{-1}. In other studies, Ni-O and Ni-N stretching vibrations for Ni(II) complexes derived from 4,5-Dichloro-o-phenylenediamine and 3,5-Dichloro-2-hydroxyacetophenone and from aspartateguanido acetate nickel (II) complex were also reported at 629, 630 cm^{-1} [94] and 611 cm^{-1} [95], respectively, in the FT-IR spectrum.

3.3. ^{1}H NMR analyses

The chemical shift values in experimental and theoretical ^{1}H NMR of complexes **1** and **2** are listed in Table 5, and the spectra are presented in Fig. 5.

In the ^{1}H NMR spectra of the starting materials, cis/trans isomer peaks for –OH protons were observed at 11.60/10.88 ppm and 11.70/10.87 ppm for **L1** and **L2,** respectively. Peaks corresponding to the NH_2 group appeared at 6.93 (for **L1**)/6.94 (for **L2)** ppm, while the *syn/anti* isomer peaks of the imine group were detected at 8.47/8.35 ppm and 8.40/8.37 ppm. Peaks associated with the aromatic ring were identified in the range of 7.56–6.89 ppm.

The experimental chemical shift values of H atoms in the rings of complex **1** were measured as (H2/H15) 6.74/6.68 ppm, (H3/H14) 7.48/7.32 ppm, (H4/H5) 6.99/6.94 ppm, and (H5/H12) 7.78/7.57 ppm (Fig. 5a). The theoretical values corresponding to these chemical shifts were calculated as 7.67/7.72, 7.98/8.11, 7.29/7.34, and 7.91/7.72 ppm, respectively. Following chelation, the –OH and $–NH_2$ proton signals of the ligand disappeared, and two imine peaks were observed at 8.55 ppm for the $CH{=}N^1$ group and 8.32 ppm for the $CH–N^4$ group, which were theoretically monitored at 9.23 and 8.96 ppm, respectively. In addition, the experimental chemical shift values for H16, H17, and H18 atoms in the S1-CH_3 group were observed at 2.74 ppm. Theoretical values for H16 and H17 atoms were calculated at 3.23 ppm, and the value for the H18 atom was calculated at 2.90 ppm.

The experimental chemical shift values of the H atoms in the rings of complex **2** were measured as (H2/H17) 6.75/6.69 ppm, (H3/H16) 7.49/7.33 ppm, (H4/H15) 7.00/6.94 ppm, and (H5/H14) 7.79/7.59 ppm (Fig. 5b). The theoretical values corresponding to these chemical shifts were calculated as 7.69/7.72 ppm, 7.98/8.11 ppm, 7.29/7.34 ppm, and 7.93/7.98 ppm, respectively. Following chelation, the –OH and $–NH_2$ proton signals of the ligand disappeared, and two imine peaks were observed at 8.56 ppm for the $CH{=}N^1$ group and 8.38 ppm for the $CH{=}N^4$ group, which were theoretically resonated at 9.23 and 9.01 ppm, respectively. In addition, the experimental chemical shift values for H18/H19 and H20/H21 atoms in the S1-CH_2-CH_2-CH_3 group were recorded as 2.29 and 1.78 ppm. Also, the value for H22, H23, and H24 atoms of the CH_3 group was measured as 0.86 ppm. In theoretical calculations, the results for H18, H19, H20, H21, H22, H23, and H24 atoms were found to be 3.95, 3.27, 2.51, 2.01, 1.51, 1.78, and 1.51 ppm, respectively.

3.4. UV–Vis analyses

UV–Vis spectral analyses of **1** and **2** were performed by recording their experimental spectra and by using theoretical calculation methods. The experimental UV–Vis. spectra are presented in Fig. 6. The wavelengths of the absorption peaks in the experimental spectrum, corresponding to the wavelengths obtained from theoretical values and calculations, are presented in Table 6. In addition, the percentages of major electronic transitions contributing to the formation of these absorption peaks and the energy values of these transitions are also provided in Table 6.

The UV–Vis. spectra of the **L1** and **L2** displayed three distinct bands at 239.5 nm, 304.5 nm, and 334 nm, corresponding to $\pi \rightarrow \pi^*$, $n \rightarrow \sigma^*$, and $n \rightarrow \pi^*$ transitions, respectively. These transitions are attributed to the phenol ring, azomethine group, and thioamide group. In the UV–Vis. spectra of **1** and **2**, absorption bands were observed at 240/239.5 nm, 301/301.5 nm, 323.5/325.5 nm, 397.5/397 nm, 471.5 nm, and 552 nm for **1** and **2**, respectively. A comparison between the spectra of the ligands and the complexes indicates that the bands in the 301–324 nm range can be attributed to intra-ligand $\pi \rightarrow \pi^*$ and $n \rightarrow \sigma^*$ transitions, while the bands at 397 and 471 nm are associated with charge transfer transitions. The weak absorptions at 552 nm in the complexes are likely

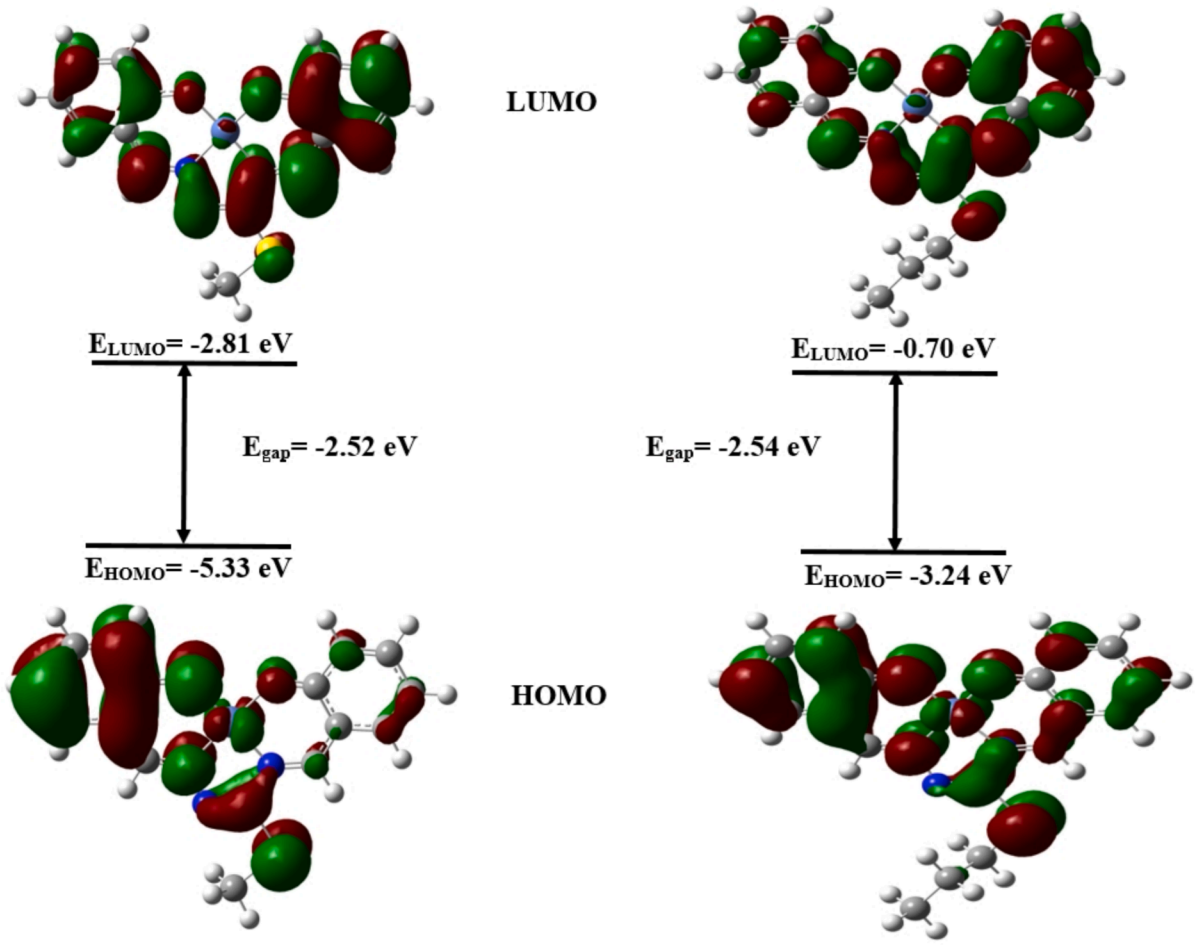

Fig. 7. Frontier molecular orbital distributions of **1** and **2**.

due to Laporte-forbidden *d–d* transitions.

It was determined that the theoretical UV–Vis spectra for **1** and **2** exhibit signals at 502 and 429 nm. The main contributions for these electronic transitions come from the HOMO → LUMO and HOMO-1 → LUMO transitions, respectively.

3.5. Frontier molecular orbitals analyses (FMOs)

To explain the chemical reactivity of a molecule, it is necessary to determine the energy gap between the HOMO and LUMO orbitals, which are known as the electron donating and electron accepting capacity, respectively [96]. The smaller the energy gap of a molecule, the better the chemical reactivity, polarizability, and softness it has. In addition, this electronic absorption represents the transition from the lowest energy state to the first excited state. In other words, it corresponds to the electron transition from the highest occupied molecular orbital (HOMO) to the lowest unoccupied molecular orbital (LUMO) [97]. The energy values of the HOMO and LUMO orbitals of both synthesized structures and the energy values of other quantum chemical properties derived from these energy values (with their formulas) are presented in Table 7 [98]. Also, Fig. 7 shows how the distributions of the **1** and **2** change when an electron is transferred from the HOMO orbital to the LUMO orbital.

The E_{HOMO} and E_{LUMO} energies calculated for **1** are −5.33 and −2.81 eV, respectively. The energy gap for this complex is found to be 2.52 eV. The E_{HOMO} and E_{LUMO} values for **2** are calculated as −3.24 and −0.70 eV, while the energy gap is found to be 2.54 eV. The addition of methyl and propyl groups to the sulfur atoms in the structures has changed the energy values of the HOMO and LUMO orbitals. The energy values of the HOMO and LUMO orbitals of the complex with the methyl added are more negative than those of the complex with the propyl group added. However, no significant difference was observed between the energy gap values. Chemical hardness values were calculated as 1.26 and 1.27 eV, and chemical softness values were calculated as 0.80 and 0.79 eV for **1** and **2**. Chemical potential values for both complexes were found as −4.07 and −1.97 eV, respectively. Additionally, the global electrophilic indices (as strong electrophiles with $\omega > 1.5$ eV) of both structures were calculated as 6.60 for **1** and 1.52 for **2**. According to the results, it was determined that the chemical reactivity of these complexes was low. It has been stated in the literature that organic and inorganic structures with energy values in this range have low reactivity and are chemically stable. In addition, the negative chemical potential values and the fact that the global hardness values are greater than the global softness values indicate that these complexes tend to remain chemically stable [99,100].

3.6. MEP analyses

The molecular electrostatic potential surface (MEP) map is a valuable instrument that predicts the electrophilic and nucleophilic regions of a molecule, as well as providing information on its chemical stability and reactivity [101]. The map depicts electron densities in various colors. The electron-rich region (electrophilic) is denoted by the red color, whereas the electron-poor region (nucleophilic) is denoted by the blue color. Neutral regions are represented by green, while slightly electron-rich regions are represented by yellow [102]. MEP maps of the

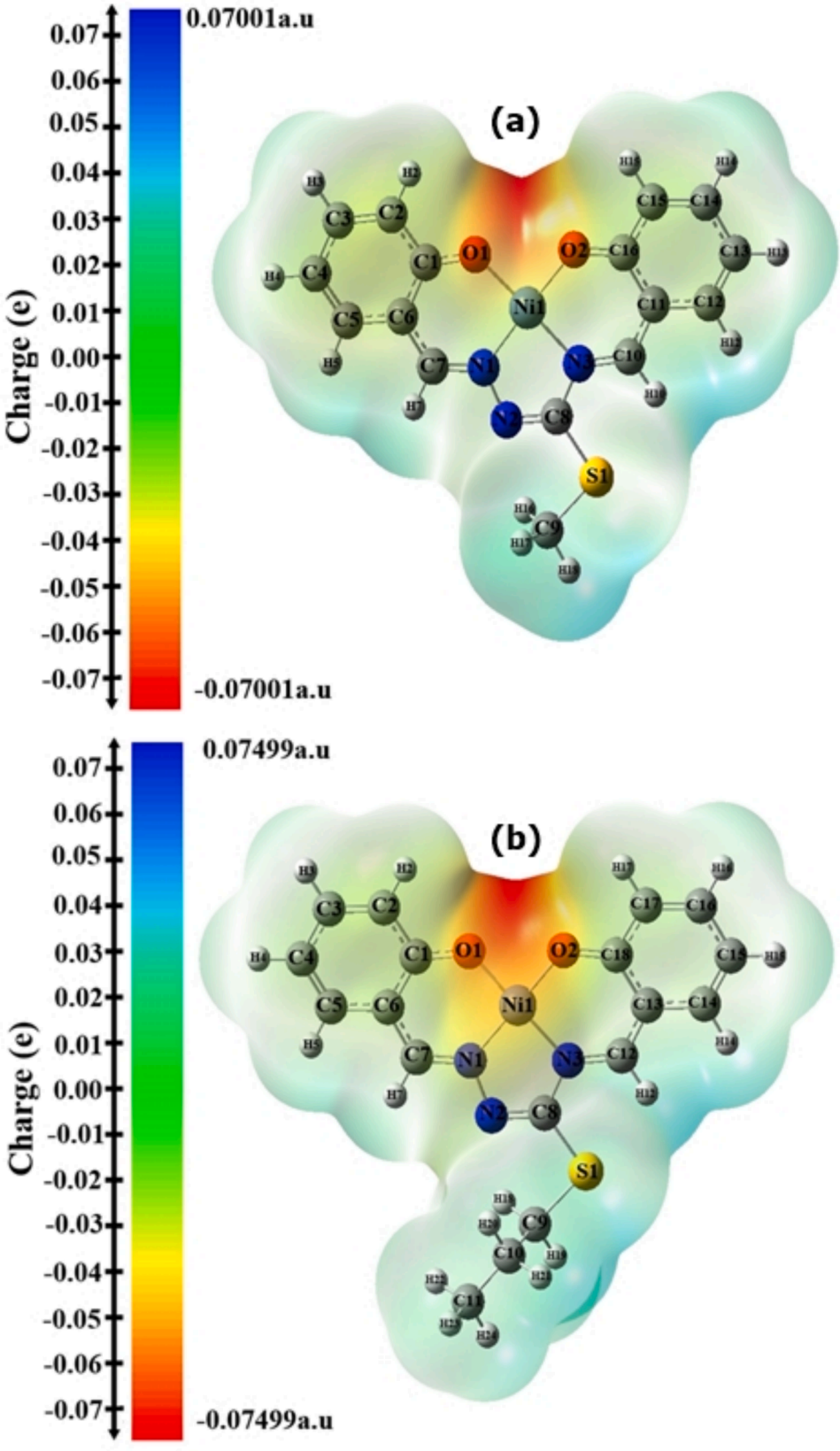

Fig. 8. Molecular electrostatic potential surface maps of **1** (a) and **2** (b).

Table 8
Topological parameters of the BCP, RCP and NRCP for both Ni(II) complexes.

Compounds	Interactions	$\rho(r)$	$\nabla^2\rho(r)$	$H(r)$	$G(r)$	$V(r)$	E_{int}(kcal/mol)	$\lvert V(r)\rvert/G(r)$	ε
1	Ni-N_5	0.12875	0.59250	−0.00441	0.19228	−0.23644	−74.1831	1.22966	0.02719
	Ni-N_6	0.12056	0.57841	−0.00380	0.18269	−0.22077	−69.2666	1.20844	0.04183
	Ni- O_3	0.10937	0.68007	−0.00166	0.18664	−0.20328	−63.7791	1.08915	0.12653
	Ni-O_4	0.10514	0.67155	−0.00144	0.18231	−0.19673	−61.7242	1.07909	0.13491
	C_{25}-H_{26}….S	0.14526	0.56891	0.00226	0.11954	−0.96869	−303.926	8.10348	0.65896
	RCP1	0.19819	0.15788	0.00926	0.30208	−0.20946	–	0.69339	−1.18766
	RCP2	0.19662	0.15624	0.00919	0.29864	−0.20668	–	0.69207	−1.18878
	NRCP1	0.15716	0.91808	0.00417	0.18775	−0.14599	–	0.77757	−1.25784
	NRCP2	0.33571	0.21403	0.00789	0.45614	−0.37772	–	0.82807	−1.40752
	NRCP3	0.15509	0.90530	0.00411	0.18514	−0.14395	–	0.77751	−1.26482
	NRCP4	0.14165	0.72959	0.00371	0.14523	−0.10807	–	0.74413	−2.12902
2	Ni-N_5	0.12883	0.59354	−0.04419	0.19258	−0.23678	−74.28972	1.22951	0.02747
	Ni-N_7	0.12064	0.57796	−0.03816	0.18266	−0.22083	−69.28541	1.20896	0.04158
	Ni- O_4	0.10521	0.67211	−0.01445	0.18248	−0.19693	−61.78678	1.07918	0.13542
	Ni-O_5	0.10939	0.68040	−0.01663	0.18674	−0.20337	−63.80733	1.08905	0.12638
	N_6….H_{26}	0.83383	0.29303	0.01074	0.62510	−0.51762	−162.4032	0.82805	0.75373
	C_{31}-H_{32}….S	0.14949	0.57198	0.02185	0.12114	−0.99284	−311.5035	8.19580	0.55427
	RCP1	0.19962	0.15624	0.00919	0.29864	−0.20667	–	0.69203	−1.18870
	RCP2	0.19821	0.15788	0.00926	0.32010	−0.20948	–	0.65442	−1.18754
	NRCP1	0.15502	0.90436	0.00411	0.18497	−0.14386	–	0.77774	−1.26454
	NRCP2	0.33555	0.21431	0.00793	0.45646	−0.37713	–	0.82620	−1.40644
	NRCP3	0.15724	0.91845	0.00417	0.18783	−0.14606	–	0.77761	−1.25791
	NRCP4	0.14459	0.74980	0.00380	0.14943	−0.11141	–	0.74556	−2.01391
	NRCP5	0.18613	0.32953	0.00155	0.66864	−0.51346	–	0.76791	−2.07068

D (Å): Distance; ρ(r) (a.u.): Density of electrons; $\nabla^2\rho(r)$ (a.u): Laplacian of electron density; V(r) (a.u): Potential energy density; (Eint) (kcal/mol): Interaction energy, ε: Ellipticity,
RCP: ring critical point, NRCP: new ring critical point.

title complexes are presented in Fig. 8. When the MEP maps of **1** and **2** were examined, the red electrophilic regions with the most negative charge values were determined around the O1 and O2 atoms. N1, N2, and N3 atoms in both complexes are in the yellow region and are located in the slightly electron-rich region. In **1**, the S1 atom and the C9 atom were bound to this atom, and in **2**, the S1 atom and the C9, C10, and C11 atoms bound to this atom were found in the blue nucleophilic region. Moreover, the C1, C6, C7, C10, C11, and C16 atoms in the **1**, and the C1, C6, C7, C10, C11, and C16 atoms in the **2** are situated in the yellow region, which is a slightly electron-rich region. Ni1 atoms coordinated with N and O atoms in both complexes are in the yellow region and are located in the slightly electron-rich region.

3.7. Atomic charge analyses

Understanding atomic charges in a molecule is crucial because they influence electronic structure, molecular polarizability, dipole moment, and other molecular properties [103]. Additionally, charge analysis is widely used to determine the electrophilic and nucleophilic attack sites of the molecule, such as the results obtained from the MEP map [104]. Table S1 illustrates the distribution of atomic charges (APT, Hirshfeld, and Natural) in both complexes. In terms of atomic charges, the Ni ion has the highest positive charge. The negative charges of the O and N atoms create the coordination environment around the metal center.

As can be seen from the ATP values in Table 8; high positive charges on atoms indicate that the atom has fewer electrons, that is, the electron density of the atom is low. Similarly, the high positive charges on C1 (0.522), C7 (0.854), C8 (0.990), C10 (0.889), C16 (0.541) atoms are due to the flow of electron density in these atoms towards the electronegative nitrogen and oxygen atoms next to them. Therefore, the electrons accumulated on electronegative oxygen and nitrogen atoms caused a higher negative charge on these atoms. On the other hand, since the electron density on the nickel atom flows towards the oxygen and nitrogen atoms that nickel coordinates, nickel has a positive charge, and since oxygen is more electronegative than nitrogen, it has a more negative charge than nitrogen. Regions with higher atomic charges indicate that the atoms interact with each other with more electrostatic attraction.

The atoms O1, O2, N1, N2, and N3 of **1** and **2** have negative values in all charge analyses. The atom S1 has a negative value in the APT and Hirshefeld analyses but a positive value in the NBO analysis. While all the H atoms of **1** are positive, some of the H atoms of **2** have very small negative values only in the APT charge analysis. All other H atoms are positive, like those of the **1**. When the results obtained from the charge analyses were compared with the MEP maps presented in Fig. 8, similar results were obtained. In other words, the results obtained from the load analyses support the MEP map.

3.8. Fukui function analyses

The Fukui function provides a comprehensive understanding of the ability of atoms within a molecule to donate or accept electrons [105]. The local selectivity of a molecule with respect to nucleophilic, electrophilic, and radical attacks can be determined by Fukui functions calculated for Hirshfeld charges using the following equations:

$$f_k^- = q_k(N) - q_k(N-1) \quad \text{(electrophilic attack)} \tag{2}$$

$$f_k^+ = q_k(N) + 1 - q_k(N) \quad \text{(nucleophilic attack)} \tag{3}$$

$$f_k^{-0} = \left(\frac{1}{2}\right)[q_k(N+1) - q_k(N-1) \quad \text{(neutral attack)} \tag{4}$$

While qk in these formulas represents the total charge of the rth atom, *qkN*, *qk(N + 1)*, and *qk(N-1)* represent the charge values of the molecule in its neutral, anionic, and cationic states [106].

The value obtained from the result of the following equation is known as the dual descriptor and allows a clear distinction to be made between electrophilic and nucleophilic regions. If the value obtained from this formula $\Delta f(r) > 0$, the atom is in an electrophilic region and is exposed to nucleophilic attacks. If $\Delta f(r) < 0$, the atom is in a nucleophilic region and is exposed to electrophilic attack [107].

$$\Delta f(r) = f^+(r) - f^-(r) \tag{5}$$

The Fukui functions and dual descriptor values calculated for **1** and **2**

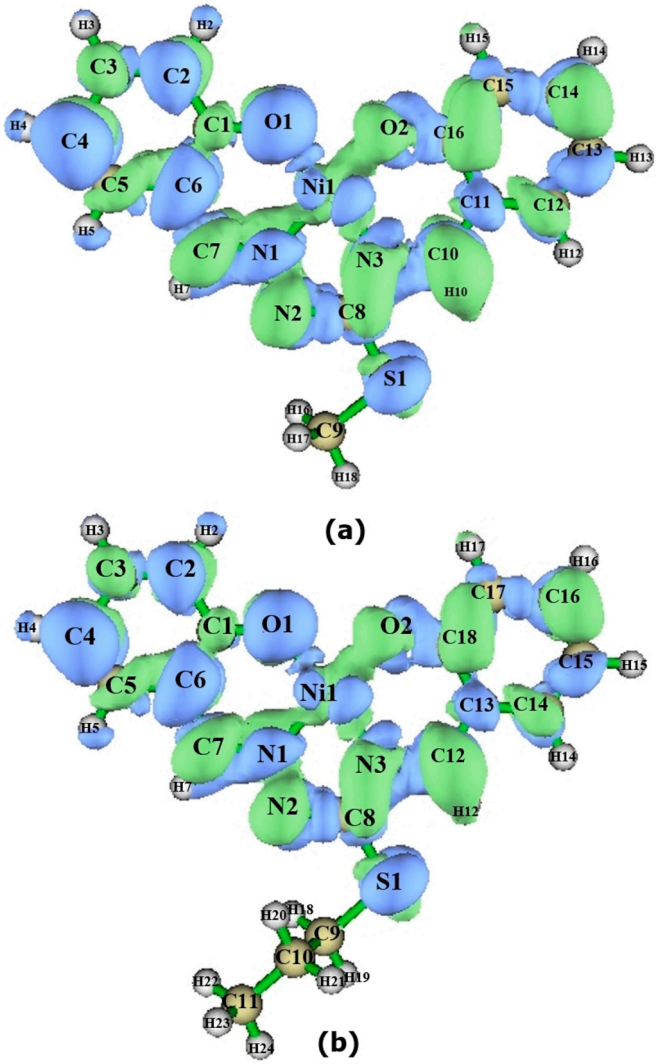

Fig. 9. Dual descriptor maps obtained from Fukui functions were calculated from the Hirshfeld charges of the **1** (a) and **2** (b).

are presented in Table S2, while the maps of the dual descriptors created using the Multiwfn program are presented in Fig. 9. In this map, the blue color indicates electrophilic regions, and the green color indicates nucleophilic regions. The results obtained from the calculations made at the DFT/HSEH1PBE/cc-pvdz + LanL2DZ level of theory presented in Table S2 and the visual results in Fig. 9 obtained from the Multiwfn program are compatible with each other. In the calculations, especially O1, N1, C4, and C6 atoms were found in the electrophilic region for **1** and **2**. The dual descriptor results obtained for Ni1 and S1 atoms were positive, and these atoms were found in the electrophilic region. Although the values obtained for Ni1 and S1 atoms do not agree with the charge analyses, the surroundings of the Ni1 atom are yellow in MEP maps. This was defined as being in a slightly electron-rich region.

3.9. Non-covalent intermolecular interactions

3.9.1. Atoms in molecules analysis (AIM)

The topological analysis of the atoms in the molecule (AIM) was used to determine the compound's bonding and non-covalent interactions, such as hydrogen and intermolecular interactions. The electron density (ρ) at the bond critical point differentiates covalent and non-covalent interactions (BCP) [108]. In our study, the different intermolecular interactions stabilizing the studied metal complexes were explored with the topological analysis of the electron, within the conceptual framework of the quantum theory of atoms in molecules (QTAIM). The properties of BCPs are significantly influenced by the topological parameters, including the electron density $\rho(r)$, the Laplacian $\nabla^2\rho(r)$, the kinetic energy densities $G(r)$, the potential $V(r)$, the total energy densities $H(r)$, and the bond energy E ($E_{int} = V(r)/2$), as proposed by Espinosa [109]. The topological analysis was applied to study the intra- and inter-molecular interactions in **1** and **2**. The various bond critical points (BCPs), new ring critical points (NRCPs), and ring critical points (RCPs) were identified and shown in Fig. 10. The calculated topological parameters were also listed in Table 8. The maximum nonbonded association for the highest energy 303.92 and 311.50 kcal/mol for **1** and **2** suggests the existence of interactions between the intermolecular bonds of hydrogen, which is supported by structural evidence studies for C31-H32…S and C25-H26…S, respectively. According to AIM theory, these interactions characterize weak H-bonds, $\nabla^2\rho(r) > 0$ and $H(r) > 0$, and are mainly electrostatic in nature. It also clearly shows how weak C-H···S

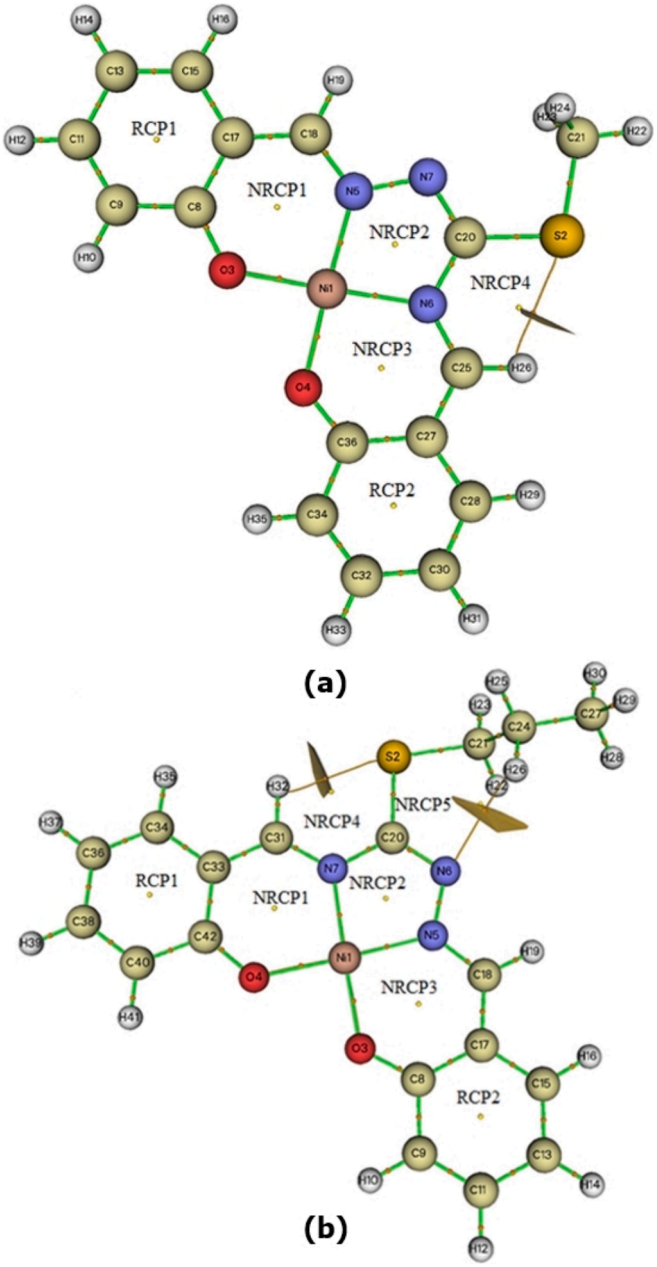

Fig. 10. AIM molecular graph showing the different BCPs, RCPs and NRCPs in **1** (a) and **2** (b).

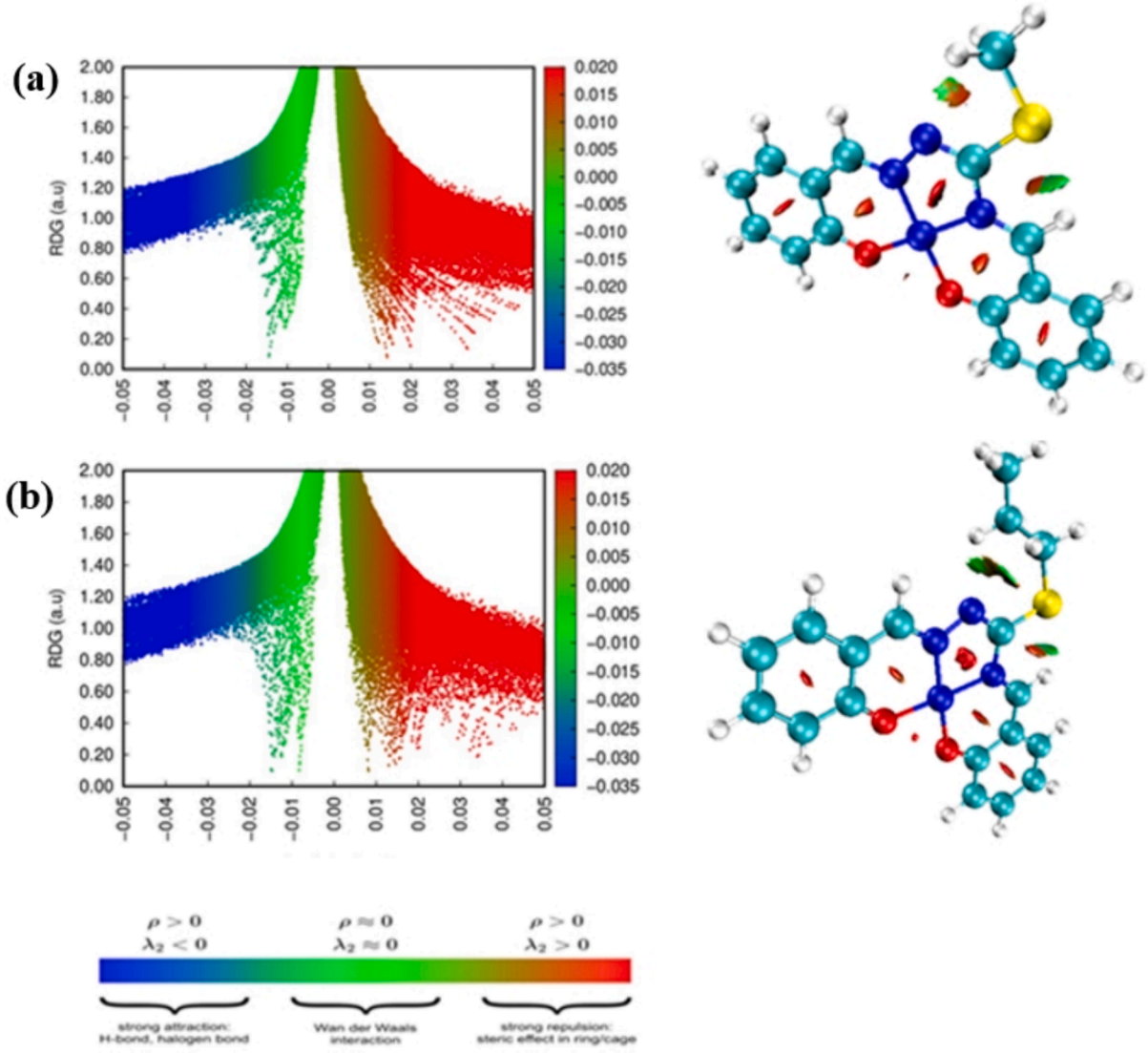

Fig. 11. 2D scatter and isosurface density plots illustrating the non-bonded interactions of **1** (a) and **2** (b) (aimm3).

bonding links the cation and anion layers. These weak interactions contribute to the stabilization of substances within the binding pocket for investigating enzymes.

Significant BCPs were observed between the metal ion and nitrogen and oxygen atoms (Ni-N, Ni-O). The values of $\rho(r)$ for all bonds were small (10^{-1} a.u.), with $\nabla^2\rho(r) > 0$, ranging from + 0.57796 a.u. to + 0.6840 a.u. for **2** and from + 0.57841 a.u. to + 0.6804 a.u. for **1**. At the same time, $H(r) < 0$, and the $|V(r)|/G(r)$ ratio was found to be 1.2, which characterizes the closed-shell interactions, including the highly polar covalent character of the studied bonds. In both complexes, the low ellipticity values at the RCP points confirm the delocalization of electrons in the aromatic nucleus. In addition, the high ellipticity values indicate a strong delocalization in the NRCP structures. All RCPs and NRCPs related to $\rho(r)$ and $\nabla^2\rho(r)$ values are positive, so we can talk about of charge concentrations around these points.

3.9.2. Non-covalent interaction-reduced density gradient (NCI-RDG)

The reduced density gradient (RDG) is highly effective for assessing non-covalent interactions (NCI) [110]. Johnson et al. devised an approach to discover and visualize weak interactions in molecular systems, including van der Waals, hydrogen bonds, and steric effects [111]. This method is a representation of a fundamental dimensionless quantity in DFT that characterizes the electron distribution deviation [112]. The results of the 2D and 3D RDG plots in Fig. 11 distinguish the nature of intra/intermolecular interactions. The isosurfaces elucidate the various types of NCI in real space via color codes. The van der Waals interactions are diminished in the regions highlighted in green, whereas the steric impact is more pronounced in the locations outlined in red and illustrated. From the 2D scatter plots, red spikes in the scatter chart between 0.005 and 0.020 a.u. confirm the strong steric influence that is suggested by red flaky patches in the core of the new ring critical points and ring critical points on the RDG isosurface. Moreover, the green plates with slight brown located between the anionic and cationic entities are attributed to Van der Waals interactions related to repulsive interactions.

3.9.3. The electron localization function (ELF) and localized orbital Locator analyses

The Electron Localization Function (ELF) and Localized Orbital Locator (LOL) are executed using the Multiwfn software program. The ELF and LOL maps are effective for identifying the locations of bond pairs, lone pairs, and the dimensions of the bonding in the compounds. The color map of ELF and LOL provides information on the distribution of electron density charge [113]. The ELF map is within the range of 0.0 to 1.0. In the ELF map, the white hue signifies the maximum limit of the ELF scale (1.0), while the medium range (0.5) is denoted by yellow to

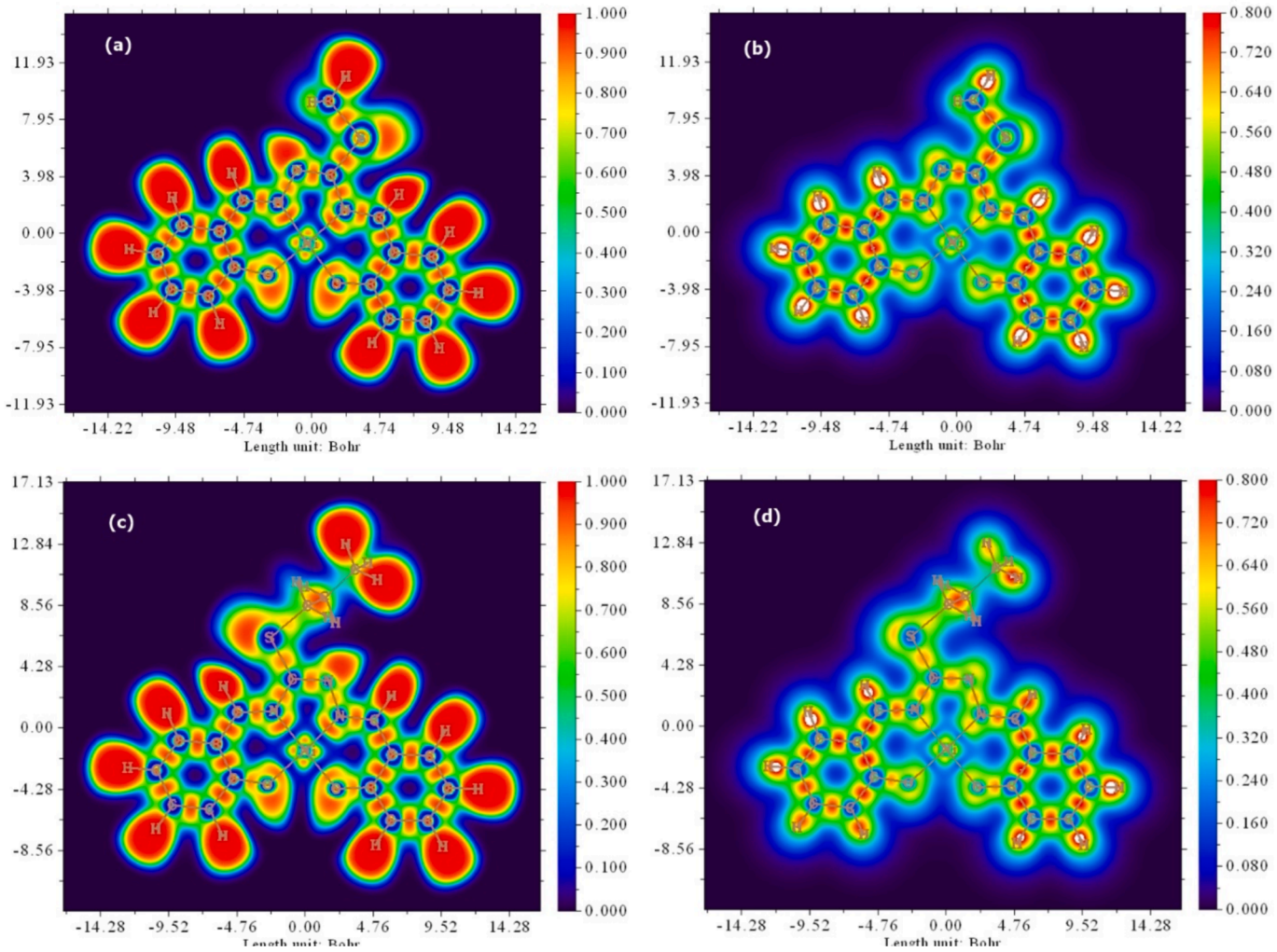

Fig. 12. The ELF (a and c) and LOL (b and d) maps of the **1** and **2**. a and b for **1**c and d for **2.**

Table 9
Molecular docking results of the **1** and the **2** with anticancer receptors.

Donor	Receptor	H-Bonded residues	Bonded distance (< 3Å)	Hydrophobic interactions (< 4 Å)	Inhibition constant K_i (μM)	Binding energy (kcal/mol)
I	Liver cancerHepG-2 (PDB ID: 2OH4)	CYS 917	2.39	LEU 838 VAL 897 VAL 914 PHE 916 PHE 1045	16.95	−10.88
	Breast cancer cellsMCF-7 (PDB ID:3W2S)	GLY 857	2.87	PHE 723 LEU 747 GLU 749 ASP 837 ALA 859 LEU 862	446.49	−8.66
2	Liver cancerHepG-2 (PDB ID: 2OH4)	LYS 866	2.47	VAL 846 LYS 866 VAL 914 ILE 1042 ASP 1044	67.67	−9.78
	Breast cancer cellsMCF-7 (PDB ID:3W2S)	GLY 857	2.85	PHE 723 LEU 747 ARG 836 ASP 837 ALA 859 LEU 862	185.30	−9.08

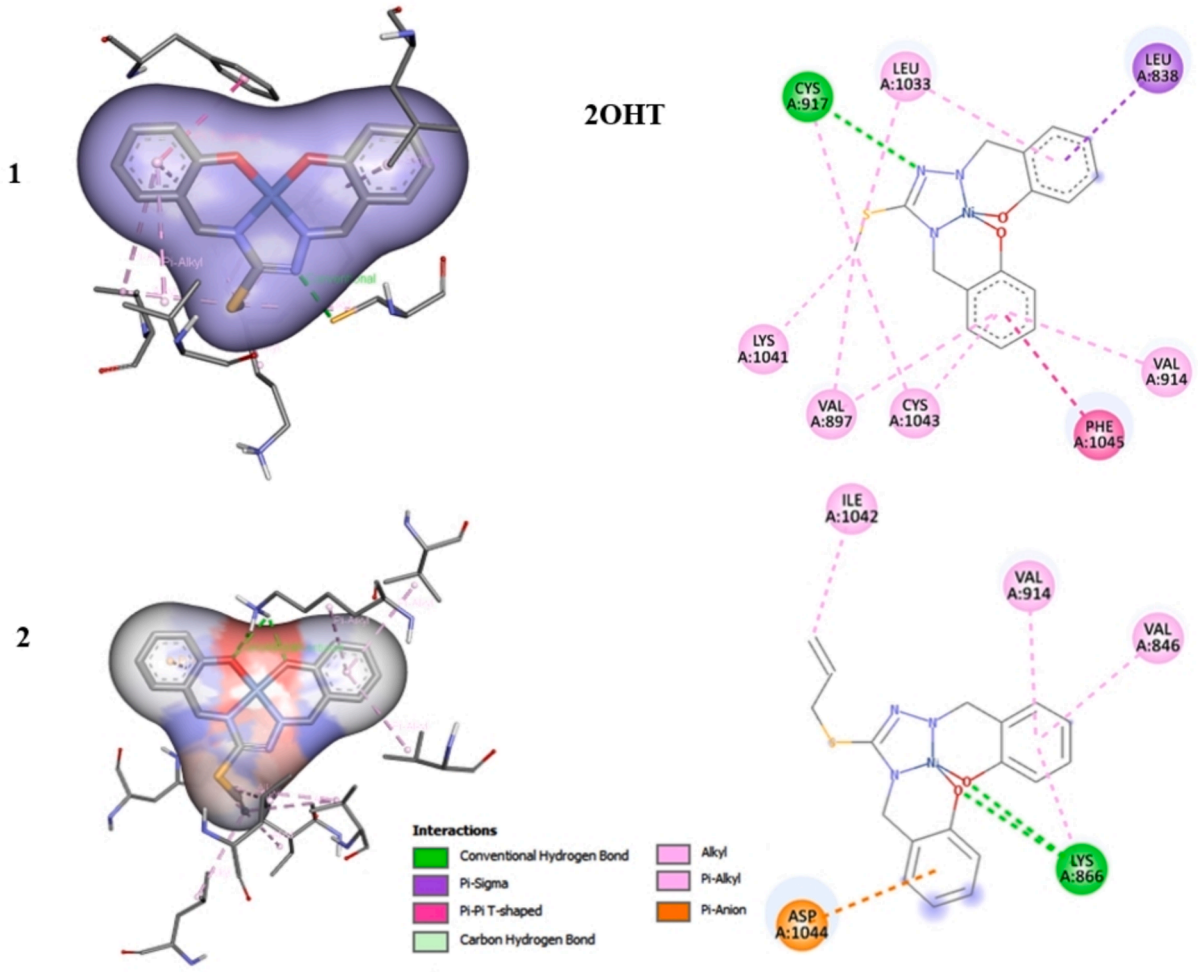

Fig. 13. Molecular docking visual of **1** and **2** with 2OHT protein.

green, and blue represents the lower limit of the ELF scale. In the color map, fully delocalized electron regions are represented by lower values of ELF (<0.5), whereas higher ELF values (ELF = 1.0) denote localized electron regions associated with nonbonding and bonding interactions. ELF and LOL values are comparable [114]. The ELF and LOL maps designed for **1** and **2** are presented in Fig. 12 (**a** and **c**) illustrate the elevated electron localization function (ELF) areas surrounding the hydrogen atom, signifying a high concentration of localized bonding and non-bonding electrons. Also, the delocalization cloud is illustrated by the blue zone around the oxygen, nitrogen, carbon, and sulfur atoms. The LOL maps presented in Fig. 12 (**b** and **d**) also present similar results as the ELF images.

3.10. Molecular docking

Molecular docking studies are an important part of computational drug design because they assess the inhibitory potential of compounds in enzyme pockets and anticipate the binding mode or mechanism of the moieties in the pockets [115]. In order to predict the affinity and binding capabilities of two molecules, computational chemistry implements an algorithmic approach known as molecular docking [116]. This approach helps with the rational creation of new anti-cancer drug classes by providing crucial information about the drug-binding mechanism in the active site [117]. Thiosemicarbazone derivatives are an effective drug in the treatment of cancer, and it also has a good affinity to bind with metals, which act on certain pathways in the cell. In this study, docking analysis was carried out with selective pharmacological targets such as aromatase enzymatic proteins of human hepatocarcinoma (HepG2) and human breast (MCF-7) cancer, which are involved in the pathogenesis and induction of cancer. MCF-7 cells are a well-known model of estrogen receptor-positive breast cancer. MCF-7 (PDB ID: 3W2S) was chosen for docking simulations because it is highly relevant to breast cancer pharmacology, particularly for evaluating drugs with estrogenic or antiestrogenic actions that may alter breast cancer cell growth. HepG-2 (PDB ID: 2OH4) is obtained from hepatocellular carcinoma and is mostly used to investigate liver cancer. This cell line exhibits a number of liver-specific activities, making it useful for investigating drug metabolism and its effects on liver cancer cells. For molecular docking experiments using cell lines such as MCF-7 and HepG-2, binding sites are frequently chosen based on known targets in these cells that are required for cancer cell survival and proliferation.

Based on the bond type and lengths formed by the synthesized compounds and target proteins, molecular docking calculates the binding energy values, which Table 9 provides; see compound interactions in Fig. 13 and Fig. 14. The more negative relative binding energy of a candidate suggests more ability to bind to the protein docking pose, and therefore more inhibition efficiency to reduce the growth of the cancer cell lines. Binding energy (E_i) and constant inhibition (Ki) were used as parameters to analyze the interaction between them. The most potent inhibitor is indicated by the lowest E_i and Ki [118,119]. The results of this analysis indicate the ability of compounds to inhibit enzyme activity, commonly called inhibitors. When we look at the interaction results, the activity of both Ni(II) complexes against HepG-2 (PDB ID: 2OH4) is better than MCF-7 (PDB ID: 3W2S) because it

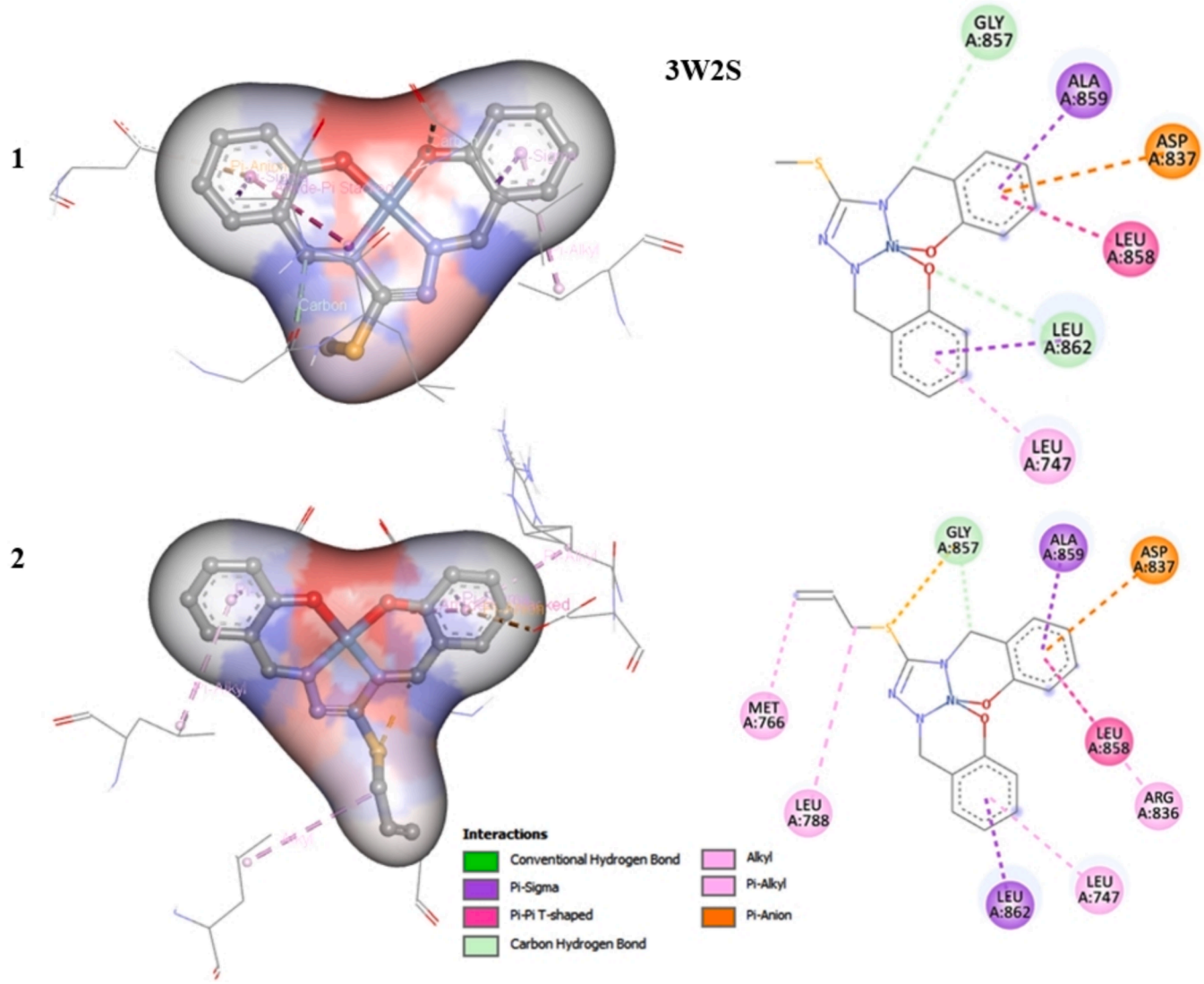

Fig. 14. Molecular docking visual of **1** and **2** with 3W2S protein.

showed the lowest binding energy and inhibition constant. As a glance at Table 9, title complexes exhibit interaction with HepG-2 via hydrogen bond LYS866→(C=N) and CYS7 917→(C=N), which were found to be lower than 3.0 Å in most cases, can be taken as evidence for true docking scores as reported in the literature. Whereas the complexes' interaction with MCF-7 occurred through the hydrogen bond GLY 857 residues. Since chemotherapeutic therapy is one of the most important and well-known procedures to treat tumors, our study evaluated the antitumor effect of newly synthesized metal complexes against two significant types of malignancy, human hepatocellular carcinoma cells (HepG-2 cells) and breast cancer cell line (Mcf-7 cells), using the molecular docking method.

4. Conclusion

Complex **1** and complex **2** were synthesized by the reaction of S-alkyl-salicylaldehyde-isothiosemicarbazones with 2-aminopyridine in the presence of $NiCl_2$, in contrast to the conventional template synthesis. Instead of coordinating with the metal as a co-ligand in the reaction, 2-aminopyridine decomposed the S-alkyl-salicylaldehydeisothiosemicarbazone compound into its constituent salicylaldehyde and S-alkyl-thiosemicarbazide. In the presence of $NiCl_2$, in the same vessel and simultaneously, the decomposed salicylaldehyde bonded to both amine ends of thiosemicarbazide, forming a chelate and simultaneously coordinating to nickel via *O,O,N,N* atoms. In the crystal structure of the two square-planar nickel(II) complexes, $\pi\cdots\pi$ stacking interactions are responsible for stabilization. Experimental FT-IR, NMR, and UV–Vis spectra of the synthesized complexes were recorded, and their theoretical values were reproduced by the DFT method and compared with each other. In addition, electronic properties (MEP, atomic charge, Fukui functions, ELF, and LOL maps) and chemical reactivity of complexes 1 and 2 were explained using quantum chemical calculation methods. In addition, topological studies were carried out to determine the basic binding sites and weak interactions of the complexes. With these analyses, electrophilic and nucleophilic regions of the structures were determined, and the regions where they can enter into chemical reactions in molecular docking studies were determined. The fact that the energy difference between the HOMO and LUMO orbitals is not too high allows these complexes to be used in biological activity studies. Molecular docking studies were carried out for liver and breast cancers. According to the obtained results, it was evaluated that both complexes could be effective in the treatment of these two cancer types.

CRediT authorship contribution statement

Ceyhun Kucuk: Writing – original draft, Formal analysis. **Elif Avcu**

Altıparmak: Writing – original draft, Validation, Data curation. **Sibel Celik:** Writing – original draft, Visualization, Software. **Işın Kılıç-Cıkla:** Writing – original draft, Software, Formal analysis. **Namık Özdemir:** Writing – original draft, Visualization, Formal analysis, Data curation. **Tülay Bal-Demirci:** Writing – original draft, Methodology, Investigation, Formal analysis, Conceptualization.

Declaration of competing interest

The authors declare that they have no known competing financial interests or personal relationships that could have appeared to influence the work reported in this paper.

Appendix A. Supplementary data

Supplementary data to this article can be found online at https://doi.org/10.1016/j.inoche.2025.114283.

Data availability

The authors are unable or have chosen not to specify which data has been used.

References

[1] T.S. Lobana, R. Sharma, G. Bawa, S. Khanna, Bonding and structure trends of thiosemicarbazone derivatives of metals—An overview, Coord. Chem. Rev. 253 (7–8) (2009) 977–1055.

[2] S. Dutta, F. Basuli, A. Castineiras, S.M. Peng, G.H. Lee, S. Bhattacharya, Variable Coordination Modes of Benzaldehyde Thiosemicarbazones – Synthesis, Structure, and Electrochemical Properties of Some Ruthenium Complexes, Eur. J. Inorg. Chem. 29 (2008) 4538–4546.

[3] R. Panico, W.H. Powell, J.C. Richer, Nomenclature of Organic Compounds, IUPAC, Blackwell: London, 105, 1993.

[4] S.R. Salman, F.S. Kamounah, Tautomerism in 1-hydroxy-2-naphthaldehyde Schiff bases: Calculation of tautomeric isomers using carbon-13 NMR, Spectroscopy 17 (4) (2003) 747–752.

[5] R.J. Fessenden, J.S. Fessenden, Organic Chemistry, 6th Edition, Brooks Cole, 1999.

[6] J.K. Lim, C.J. Mathias, M.A. Green, Mixed Bis(thiosemicarbazone) Ligands for the Preparation of Copper Radiopharmaceuticals: Synthesis and Evaluation of Tetradentate Ligands Containing Two Dissimilar Thiosemicarbazone Functions, J. Med. Chem. 40 (1) (1997) 132–136.

[7] R. Pedrido, M.R. Bermejo, M.J. Romero, M. Vázquez, A.M. González-Noya, M. Maneiro, M.J. Rodríguez, M.I. Fernández, Syntheses and X-ray characterization of metal complexes with the pentadentate thiosemicarbazone ligand bis(4-N-methylthiosemicarbazone)-2,6-diacetylpyridine. The first pentacoordinate lead(II) complex with a pentagonal geometry, Dalton Trans. 7 (3) (2005) 572–579.

[8] T. Bal-Demirci, Synthesis, spectral characterization of the zinc(II) mixed-ligand complexes of *N*(4)-allyl thiosemicarbazones and *N*,*N*,*N*′,*N*′-tetramethylethylenediamine, and crystal structure of the novel [ZnL_2(tmen)] compound, Polyhedron 27 (1) (2008) 440–446.

[9] P. Chellan, S. Nasser, L. Vivas, K. Chibale, G.S. Smith, Cyclopalladated complexes containing tridentate thiosemicarbazone ligands of biological significance: Synthesis, structure and antimalarial activity, J. Organomet. Chem. 695 (19–20) (2010) 2225–2232.

[10] E.A. Altiparmak, G. Erdemir, N. Özdemir, S.E. Kuruca, Tülay Bal-Demirci, Cu(II) salen and 1,2,4-triazole complexes from thiosemicarbazone: synthesis, physicochemical and structural properties and cytotoxic activities, New J. Chem. 44 (14) (2020) 5333–5342.

[11] J.M. Jacob, M.R.P. Kurup, K. Nisha, G. Serdaroğlu, S. Kaya, Mixed ligand copper (II) chelates derived from an O, N, S- donor tridentate thiosemicarbazone: Synthesis, spectral aspects, FMO, and NBO analysis, Polyhedron 189 (2020) 114736.

[12] P. Kalaivani, R. Prabhakaran, E. Ramachandran, F. Dallemer, G. Paramaguru, R. Renganathan, P. Poornima, V.V. Padma, K. Natajaran, Influence of terminal substitution on structural, DNA, Protein binding, anticancer and antibacterial activities of palladium(ii) complexes containing 3-methoxy salicylaldehyde-4(N) substituted thiosemicarbazones, Dalton Trans. 41 (8) (2012) 2486–2499.

[13] J.F. Machado, F. Marques, T. Pinheiro, M.J.V. de Brito, G. Scalese, L. Pérez-Díaz, L. Otero, J.P.M. António, D. Gambino, T.S. Morais, Copper(I)-Thiosemicarbazone Complexes with Dual Anticancer and Antiparasitic Activity, ChemMedChem 18 (14) (2023) e202300074.

[14] E.S. Çakmakçı, E. Subaşı, E. Öztürk, A. Şahiner, B.Ş. Yüksel, Cobalt(II), nickel(II), palladium(II) and zinc(II) metallothiosemicarbazones: Synthesis, characterization, X-ray structures and biological activity, Inorganica Chim. Acta 551 (2023) 121462.

[15] G. Domagk, R. Behenisch, F. Mietzsch, H. Schmidt, On a new class of compounds effective in vitro against tubercle bacilli, Naturwissenschaften 33 (1946) 315.

[16] J.P. Scovill, D.L. Klayman, C.F. Franchino, 2-Acetylpyridine thiosemicarbazones. 4. Complexes with transition metals as antimalarial and antileukemic agents, J. Med Chem. 25 (10) (1982) 1261–1264.

[17] A.E. Liberta, D.X. West, Antifungal and antitumor activity of heterocyclic thiosemicarbazones and their metal complexes: current status, Biometals 5 (1992) 121–126.

[18] J.J. Knox, S.J. Hotte, C. Kollmannsberger, E. Winquist, B. Fisher, E.A. Eisenhauer, Phase II study of Triapine in patients with metastatic renal cell carcinoma: a trial of the national cancer institute of Canada clinical trials group (NCIC IND.161), Invest. New Drugs 25 (2007) 471–477.

[19] V. Opletalová, D.S. Kalinowski, M. Vejsová, J. Kuneš, M. Pour, J. Jampílek, V. Buchta, D.R. Richardson, Identification and Characterization of Thiosemicarbazones with Antifungal and Antitumor Effects: Cellular Iron Chelation Mediating Cytotoxic Activity, Chem. Res. Toxicol. 21 (9) (2008) 1878–1889.

[20] G. Pelosi, F. Bisceglie, F. Bignami, P. Ronzi, P. Schiavone, M.C. Re, C. Casoli, E. Pilotti, Antiretroviral Activity of Thiosemicarbazone Metal Complexes, J. Med. Chem. 53 (24) (2010) 8765–8769.

[21] T. Bal-Demirci, G. Congur, A. Erdem, S., Erdem Kuruca, N. Özdemir, K. Akgün Dar, B. Varol, B. Ülküseven, Iron(III) and nickel(II) complexes as potential anticancer agents: synthesis, physicochemical and structural properties, cytotoxic activity and DNA interactions, New J. Chem. 39(7) (2015) 5643-5653.

[22] K.Y. Salim, S.M. Vareki, W.R. Danter, S. San Marina, J. Koropatnick, COTI-2, a novel small molecule that is active against multiple human cancer cell lines in vitro and in vivo, Oncotarget 7 (27) (2016) 41363–41379.

[23] T.A. Yousef, O.K. Alduaij, G.M. Abu El-Reash, R.M. El Morshedy, Semiempirical studies, spectral analysis, in vitro antibacterial and DNA degradation studies of heterocyclic thiosemicarbazone ligand and its metal complexes, J. Mol. Liquids 222 (2016) 762–776.

[24] T. Bal-Demirci, Ş. Güveli, S. Yeşilyurt, N. Özdemir, B. Ülküseven, Thiosemicarbazone ligand, nickel(II) and ruthenium(II) complexes based on vitamin B6 vitamer: The synthesis, different coordination behaviors and antioxidant activities, Inorg. Chim. Acta 502 (2020) 119335.

[25] B. Karpagam, M. Sankarganesh, L. Ravi, M.P. Kesavan, G.G.V. Kumar, Gurusamy Rajagopal, Jegathalaprathaban Rajesh, Synthesis, spectroscopic and crystal structure of nickel(II) complex of thiosemicarbazone basedSchiff base: Antimicrobial, anticancer and molecular docking studies, Inorg. Chem. Commun. 132 (2021) 108850.

[26] H. Yakan, Ü.M. Koçyiğit, H. Muğlu, M. Ergul, S. Erkan, E. Güzel, P. Taslimi, İ. Gülçin, Potential thiosemicarbazone-based enzyme inhibitors: Assessment of antiproliferative activity, metabolic enzyme inhibition properties, and molecular docking calculations, J. Biochem. Mol. Toxicol. 36 (5) (2022) e23018.

[27] E. Avcu Altıparmak, G. Eroğlu Özen, N. Özdemir, S.E. Kuruca, T. Bal Demirci, Synthesis, Cytotoxicities, Structural Properties and Comparison of Dihalogenosubstituted-thiosemicarbazone ligands and Mixed-Ligand Ni(II) Complexes, Dalton Trans. (2025) in press.

[28] Y. Yu, L.R. Lin, K.B. Yang, X. Zhong, R.B. Huang, L.S. Zheng, p-Dimethylaminobenzaldehyde thiosemicarbazone: a simple novel selective and sensitive fluorescent sensor for mercury(II) in aqueous solution, Talanta 1569 (1) (2006) 103–1066.

[29] A. Fihri, P. Meunier, J.C. Hierso, Performances of symmetrical achiral ferrocenylphosphine ligands in palladium-catalyzed cross-coupling reactions: A review of syntheses, catalytic applications and structural properties, Coord. Chem. Rev. 251 (15–16) (2007) 2017–2055.

[30] I.D. Kostas, B.R. Steele, Thiosemicarbazone Complexes of Transition Metals as Catalysts for Cross-Coupling Reactions, Catalysts 10 (10) (2020) 1107.

[31] S. Priyarega, J. Haribabu, R. Karvembu, Development of thiosemicarbazone-based transition metal complexes as homogeneous catalysts for various organic transformations, Inorg. Chim. Acta 532 (2022) 120742.

[32] S.A. Darwish, E.H. Aish, S.A. Elkhabiry, S.Y. Abbas, Synthesis and polyester printing applications of transition metal complexes of tridentate 5-(*m*-tolyldiazenyl)salicylaldehyde thiosemicarbazone derivatives, Phosphorus Sulfur Silicon Relat. Elem. 199 (5) (2024) 420–428.

[33] E. Avcu Altıparmak, S. Yazar, T. Bal-Demirci, A Flexible Asymmetric Supercapacitor with High-Performance and Long-Lifetime: Fabrication of Nanoworm-Like-Structured Electrodes Based on Polypyrrole-Thiosemicarbazone Complex, Small Methods (2024), 2401140 in press.

[34] C. Yamazaki, The Structure of Isothiosemicarbazones, Can. J. Chem 53 (4) (1975) 610–615.

[35] S. Güveli, N. Özdemir, B. Ülküseven, T. Bal-Demirci, Divalent nickel complexes of thiosemicarbazone based on 5-bromosalicylaldehyde and triphenylphosphine: Experimental and theoretical characterization, Polyhedron 113 (2016) 16–24.

[36] S. Güveli, A. Koca, N. Özdemir, T. Bal-Demirci, B. Ülküseven, Electrochemistry and structural properties of new mixed ligand nickel(II) complexes based on thiosemicarbazone, New J. Chem. 38 (11) (2014) 5582–5589.

[37] V.B. Arion, Coordination chemistry of S-substituted isothiosemicarbazides and isothiosemicarbazones, Coord. Chem. Rev. 387 (2019) 348–397.

[38] A. Akbari, H. Ghateazadeh, R. Takjoo, B. Sadeghi-Nejad, M. Mehrvar, J.T. Mague, Synthesis & crystal structures of four new biochemical active Ni(II) complexes of thiosemicarbazone and isothiosemicarbazone-based ligands: In vitro antimicrobial study, J. Mol. Struct. 1181 (2019) 287–294.

[39] V. Graur, I. Usataia, O. Garbuz, A. Gulea, Novel Copper(II) Complexes with S-Substituted Isothiosemicarbazone as Highly Selective Anticancer Compounds against BxPC-3 Cell Line, Med. Sci. Forum. 14 (2022) 33.

[40] F.D. Kalındemirtaş, B. Kaya, M. Bener, O. Şahin, S. Erdem-Kuruca, T. Bal-Demirci, B. Ülküseven, Iron(III) complexes based on tetradentate thiosemicarbazones: Synthesis, characterization, radical scavenging activity and in vitro cytotoxicity on K562, P3HR1 and JURKAT cells, Appl. Organomet. Chem. 35 (2021) e6157.

[41] M.S. Ali, F.A. El-Saied, M.M.E. Shakdofa, S. Karnik, L.A. Jaragh-Alhadad, Synthesis and characterization of thiosemicarbazone metal complexes: Crystal structure, and antiproliferation activity against breast (MCF7) and lung (A549) cancers, J. Mol. Struct. 1274 (2023) 134485.

[42] V. Jevtović, H. Hamoud, S. Al-Zahrani, K. Alenezi, S. Latif, T. Alanazi, F. Abdulaziz, D. Dimić, Synthesis, Crystal Structure, Quantum Chemical Analysis, Electrochemical Behavior, and Antibacterial and Photocatalytic Activity of Co Complex with Pyridoxal-(S-Methyl)-isothiosemicarbazone Ligand, Molecules 27 (2022) 4809.

[43] G. Prakash, R. Manikandan, P. Viswanathamurthi, K. Velmurugan, R. Nandhakumar, Ruthenium(III) S-methylisothiosemicarbazone Schiff base complexes bearing PPh3/AsPh3 coligand: Synthesis, structure and biological investigations, including antioxidant, DNA and protein interaction, and in vitro anticancer activities, J. Photochem. Photobiol. B 138 (2014) 63–74.

[44] J.A. Tainer, V.A. Roberts, E.D. Getzoff, Metal-binding sites in proteins, Curr. Opin. Biotechnol. 2 (1991) 582–591.

[45] V. Jevtovic, A.K. Alshamari, D. Milenković, J.D. Marković, Z. Marković, D. Dimić, The Effect of Metal Ions (Fe, Co, Ni, and Cu) on the Molecular-Structural, Protein Binding, and Cytotoxic Properties of Metal Pyridoxal-Thiosemicarbazone Complexes, Int. J. Mol. Sci. 24 (2023) 11910.

[46] S. Kumar, A. Hansda, A. Chandra, A. Kumar, M. Kumar, M. Sithambaresan, M.S. H. Faizi, V. Kumar, R.P. John, Co(II), Ni(II), Cu(II) and Zn(II) complexes of acenaphthoquinone 3-(4-benzylpiperidyl)thiosemicarbazone: Synthesis, structural, electrochemical and antibacterial studies, Polyhedron 134 (2017) 11–21.

[47] V. Jevtovic, A. Rakić, O.A.O. Alshammari, M.S. Alhar, T. Alenezi, V. Rakic, D. Dimić, Theoretical Study of the Effects of Different Coordination Atoms (O/S/N) on Crystal Structure, Stability, and Protein/DNA Binding of Ni(II) Complexes with Pyridoxal-Semi, Thiosemi, and Isothiosemicarbazone Ligand Systems, inorganics 12 (2024) 251.

[48] F. Abdulaziz, K.F. Alabbosh, O.A.O. Alshammari, W.M.B. Tuwalah, T.Y. A. Alanazi, A. Rakić, M. Barić, M. Marković, V. Jevtovic, D. Dimić, Crystallographic Structure and Quantum-Chemical Analysis of Biologically Active Co(III)-Pyridoxal–Isothiosemicarbazone Complex, Inorganics 11 (2023) 466.

[49] V. Jevtovic, N. Alshammari, S. Latif, A.K.D. Alsukaibi, J. Humaidi, T.Y.A. Alanazi, F. Abdulaziz, S.I. Matalka, N.Đ. Pantelić, M. Marković, A. Rakić, D. Dimić, Synthesis, Crystal Structure, Theoretical Calculations, Antibacterial Activity, Electrochemical Behavior, and Molecular Docking of Ni(II) and Cu(II) Complexes with Pyridoxal-Semicarbazone, Molecules 27 (2022) 6322.

[50] N.V. Gerbeleu, V.B. Arion, J. Burgess, Template Synthesis of Macrocyclic Compounds, Wiley-VCH, Weinheim, 1999.

[51] J. Gradinaru, A. Forni, V. Druta, S. Quici, A. Britchi, C. Deleanu, N. Gerbeleu, Ni (II) complexes with [N_3O] Schiff base ligands bearing S-methylisothiosemicarbazide unit: design, synthesis and structure, Inorg. Chim. Acta 338 (2002) 169–181.

[52] T. Bal, B. Atasever, Z. Solakoğlu, S. Erdem-Kuruca, B. Ülküseven, Synthesis, characterisation and cytotoxic properties of the N^1,N^4-diarylidene-*S*-methyl-thiosemicarbazone chelates with Fe(III) and Ni(II), Eur. j. med. chem. 42 (2) (2007) 161–167.

[53] Y.D. Kurt, B. Ülküseven, Unusual template condensation of benzophenone thiosemicarbazones and salicylaldehydes with nickel(II), J. Coord. Chem. 63 (5) (2010) 828–836.

[54] B. Kaya, D. Akyüz, T. Karakurt, O. Şahin, A. Koca, B. Ülküseven, Cobalt(II)/(III) complexes bearing a tetradentate thiosemicarbazone: Synthesis, experimental and theoretical characterization, and electrochemical and antioxidant properties, Appl. Organomet. Chem. 34 (11) (2020) e5930.

[55] N.V. Gerbeleu, M.D. Revenko, V.G. Rusu, K.M. Indrichan, M.A. Yampolskaya, Coordination compounds of zinc with S-substituted N^1,N^4-di(salicylidene)-isothiosemicarbazides, Russ. j. inorg. chem. 31 (5) (1986) 691–694.

[56] T. Bal-Demirci, M. Şahin, M. Özyürek, E. Kondakçı, B. Ülküseven, Synthesis, antioxidant activities of the nickel(II), iron(III) and oxovanadium(IV) complexes with N_2O_2 chelating thiosemicarbazones, Spectrochim. Acta A Mol. Biomol. Spectrosc. 126 (2014) 317–323.

[57] D. Cirri, T. Marzo, I. Tolbatov, A. Marrone, F. Saladini, I. Vicenti, F. Dragoni, A. Boccuto, L. Messori, In Vitro Anti-SARS-CoV-2 Activity of Selected Metal Compounds and Potential Molecular Basis for Their Actions Based on Computational Study, Biomolecules 11 (12) (2021) 1858.

[58] Stoe & Cie (2002). X-AREA Version 1.18 and X-RED32 Version 1.04. Stoe & Cie GmbH, Darmstadt, Germany.

[59] G.M. Sheldrick, SHELXT – Integrated space-group and crystal-structure determination, Acta Crystallogr. A 71 (2015) 3–8.

[60] G.M. Sheldrick, Crystal structure refinement with SHELXL, Acta Crystallogr. C 71 (2015) 3–8.

[61] O.V. Dolomanov, L.J. Bourhis, R.J. Gildea, J.A.K. Howard, H. Puschmann, OLEX2: a complete structure solution, refinement and analysis program, J. Appl. Crystallogr. 42 (2009) 339–341.

[62] M.J. Frisch, G.W. Trucks, H.B. Schlegel, G.E. Scuseria, M.A. Robb, J.R. Cheeseman, G. Scalmani, V. Barone, B. Mennucci, G.A. Petersson, H. Nakatsuji, M. Caricato, X. Li, H.P. Hratchian, A.F. Izmaylov, J. Bloino, G. Zheng, J.L. Sonnenberg, M. Hada, M. Ehara, K. Toyota, R. Fukuda, J. Hasegawa, M. Ishida, T. Nakajima, Y. Honda, O. Kitao, H. Nakai, T. Vreven, J.A. Montgomery, Jr., J.E. Peralta, F. Ogliaro, M. Bearpark, J.J. Heyd, E. Brothers, K.N. Kudin, V.N. Staroverov, R. Kobayashi, J. Normand, K. Raghavachari, A. Rendell, J.C. Burant, S.S. Iyengar, J. Tomasi, M. Cossi, N. Rega, J.M. Millam, M. Klene, J.E. Knox, J.B. Cross, V. Bakken, C. Adamo, J. Jaramillo, R. Gomperts, R.E. Stratmann, O. Yazyev, A.J. Austin, R. Cammi, C. Pomelli, J.W. Ochterski, R.L. Martin, K. Morokuma, V.G. Zakrzewski, G.A. Voth, P. Salvador, J.J. Dannenberg, S. Dapprich, A.D. Daniels, O. Farkas, J.B. Foresman, J. V. Ortiz, J. Cioslowski, D.J. Fox, Gaussian 09, Gaussian, Inc., Wallingford CT, (2009).

[63] H.M.A. El-Lateef, M.M. Khalaf, A.A. Amer, A.A. Abdelhamid, A. Abdou, Antibacterial, antifungal, anti-inflammatory evaluation, molecular docking, and density functional theory exploration of 2-(1H-benzimidazol-2-yl)guanidine mixed-ligand complexes: Synthesis and characterization, Appl. Organomet. Chem. 38 (1) (2024) e7299.

[64] R. Dennington, T. Keith, J. Millam, GaussView, Version 5, Semichem Inc., Shawnee Mission, KS, USA, 2009.

[65] N. Özdemir, F.D. Karabekmez, E.Ö. Karaca, N. Gürbüz, İ. Özdemir, Synthesis, crystal structure, DFT studies and catalytic activity of an N-(2,2-dimethyl-1,3-dioxolane-4yl-methyl)benzimidazole ruthenium(II) hydrate complex, J. Mol. Struct. 1281 (2023) 135159.

[66] E.A. Altiparmak, S. Yazar, N. Özdemir, T.B. Demirci, B. Ülküseven, Supramolecular Ni(II) complex aggregates with a circular linkage of intermolecular multi-hydrogen bonding frameworks based on thiosemicarbazone, and a Cu(II) complex: Synthesis, structural, DFT, Electrochemical and Antioxidant Studies, Polyhedron 209 (2021) 115457.

[67] D. Pech-Puch, J. Rodríguez, B. Cautai, C.A. Sandoval-Castro, C. Jiménez, Cytotoxic Furanoditerpenes from the Sponge Spongia tubulifera Collected in the Mexican Caribbean, Mar. Drugs 17 (2019) 416.

[68] C.A. Huerta-Aguilar, Z.J. Diaz-Puerto, E.D. Tecuapa-Flores, P. Thangarasu, Crystal Plane Impact of ZnFe2O4−Ag Nanoparticles Influencing Photocatalytical and Antibacterial Properties: Experimental and Theoretical Studies, ACS Omega 7 (2022) 33985–34001.

[69] A. Ruiz-Molina, D. Pech-Puch, R.E. Millán, L. Ageitos, H. Villegas-Hernández, J. Pachón, J.P. Sestelo, J. Sánchez-Céspedes, J. Rodríguez, C. Jiménez, Uncovering the Potent Antiviral Activity of the Sesterterpenoids from the Sponge Ircinia Felix Against Human Adenoviruses: from the Natural Source to the Total Synthesis, Chem. Eur. J. 30 (2024) e202401844.

[70] G. Bella, G. Bruno, A. Santoro, Knotted or unknotted? A theoretical quantum protocol for luminescence simulation of metallo-supramolecular knots, J. Photochem. Photobiol. A Chem. 458 (2025) 115978.

[71] N. Özdemir, E.Ö. Karaca, N. Gürbüz, İ. Özdemir, Experimental and Theoretical Charaterization of 3-(3,5-dimethylbenzyl)-1-Methyl-3,4,5,6-Tetrahydropyrimidinium Trichlorido(η6–p-cymene)Ruthenate(II), J. Struct. Chem. 64 (2023) 2167–2177.

[72] D.I. Tasgin, P.S. Sirin, A Theoretical Investigation: Effect of Structural Modifications on Molecular, Electronic, and Optical Properties of Phosphonate Substituted BODIPY Dyes, Chem. Select. 6 (19) (2021) 4677–4683.

[73] T. Lu, F. Chen, Multiwfn: a multifunctional wavefunction analyzer, J. Comput. Chem. 33 (5) (2012) 580–592.

[74] G.M. Morris, D.S. Goodwill, R.S. Halliday, R. Huey, W. Hart, R.K. Belew, A. J. Olson, Automated docking using a Lamarckian genetic algorithm and an empirical binding free energy function, J. Comput. Chem. 19 (1998) 1639.

[75] RSCB PDB Protein Data Bank. https://www.rcsb.org/.Accessed 01 January 2025.

[76] Dassault Systemes BIOVIA, Discovery Studio Modeling Environment, Dassault Systemes, San Diego, 2017.

[77] R. Yanardag, T. Bal Demirci, B. Ülküseven, S. Bolkent, S. Tunali, S. Bolkent, Synthesis, characterization and antidiabetic properties of N^1-2,4-dihydroxybenzylidene-N^4-2-hydroxybenzylidene-S-methyl-thiosemicarbazidato-oxovanadium(IV), Eur. J. Med. Chem. 44 (2) (2009) 818–826.

[78] Y. Kurt, A. Koca, M. Akkurt, B. Ülküseven, Iron(III) and nickel(II) complexes of O,N,N,O-chelating benzophenone thiosemicarbazone: Electrochemistry and *in situ* spectroelectrochemistry, Inorg. Chim. Acta 388 (2012) 148–156.

[79] M. Ahmadi, A. Fasihizad, B. Machura, R. Kruszynski, T. Barak, New complexes of an unsymmetrical tetradentate isothiosemicarbazone: Structural, spectral and thermogravimetric investigations, and their nanoparticles synthesis, Polyhedron 81 (2014) 115–122.

[80] R. Takjoo, R. Centore, A. Akbari, M. Ahmadi, Square planar nickel(II) complexes derived from 5-bromo-2-hydroxybenzaldehyde S-ethylisothiosemicarbazone: Preparation, characterization and structural studies, Polyhedron 80 (2014) 243–249.

[81] B. İlhan-Ceylan, Oxovanadium(IV) and Nickel(II) complexes obtained from 2,2'-dihydroxybenzophenone-S-methyl-thiosemicarbazone: Synthesis, characterization, electrochemistry, and antioxidant capability, Inorg. Chim. Acta 517 (2021) 120186.

[82] S. Eğlence-Bakır, New nickel(II) complexes containing N_2O_2 donor thiosemicarbazones: Synthesis, characterization and antioxidant properties, J. Mol. Struct. 1246 (2021) 131121.

[83] L. Yang, D.R. Powell, R.P. Houser, Structural variation in copper(i) complexes with pyridylmethylamide ligands: structural analysis with a new four-coordinate geometry index, τ_4, Dalton Trans. 9 (2007) 955–964.

[84] A. Okuniewski, D. Rosiak, J. Chojnacki, B. Becker, Coordination polymers and molecular structures among complexes of mercury(II) halides with selected 1-benzoylthioureas, Polyhedron 90 (2015) 47–57.

[85] A.B. Rached, W. Maalej, P. Guionneau, N. Daro, T. Mhiri, H. Feki, Z. Elaoud, Synthesis, crystal structure, and vibrational and dft simulation studies of benzylammonium dihydrogen phosphate, J. Phys. Chem. Solids. 123 (2018) 150–156.

[86] J.B. Diccianni, C. Hu, T. Diao, Bimetallic, High-Valent Nickel Complexes: Ni–Ni Bonds in Aryl– Halogen Bond Formation, Angew. Chem. Int. Ed. 56 (2017) 3635–3639.
[87] M.H. Jamroz, Vibrational energy distribution analysis (VEDA): scopes and limitations, Spectrochim. Acta A Mol. Biomol. Spectrosc. 114 (2004) 220–230.
[88] N. Özdemir, R. Fırıncı, M.E. Günay, Synthesis, Experimental and Theoretical Characterization of (μ^4-oxo)hexakis(μ^2-chloro)-tetrakis[1-(allyl)-1H-imidazole] tetracopper(II), Croat. Chem. Acta 96 (1) (2023) 1–8.
[89] W.P. Gurgel, A. Correa, C.C. Santos, A.O. Santos, G.D. Saraiva, P.T.C. Freire, C.E. S. Nogueira, S.G.C. Moreira, F.F. de Sousa, Elucidating the phase transitions of decanoic-acid crystal by XRD, Raman, group theory and Gibbs energy analyses combined with DFT calculations, Spectrochim. Acta A Mol. Biomol. Spectrosc. 287 (2) (2023) 122068.
[90] V. Krishnakumar, S. Dheivamalar, R.J. Xavier, V. Balachandran, Analysis of vibrational spectra of 4-amino-2,6-dichloropyridine and 2-chloro-3,5-dinitropyridine based on density functional theory calculations, Spectrochim. Acta A Mol. Biomol. Spectrosc. 65 (2006) 147–154.
[91] R.M. Silverstein, F.X. Webster, D.J. Kiemle, D.L. Bryce, Spectrometric identification of organic compounds, John Wiley & Sons, Singapore, 2014.
[92] G. Anand, M. Sivasubramanian, I. Manimehan, A. Ruby, R. Abinayashri, R. K. Asmitha, Synthesis, spectroscopic elucidation (FT-IR, FT-Raman, UV-vis), quantum chemical computation (PES, FMO, HOMO–LUMO, MEP, NLO, Hirshfeld) and molecular docking studies on 2-thiophenecarboxamide crystal, J. Mol. Struct. 1286 (2023) 135586.
[93] A. Kherrouba, R. BEnsegueni, M. Guergouri, A.L. Boulkedid, M. Boutebdja, M. Bencharif, Synthesis, crystal structures, optical properties, DFT and TD-DFT studies of Ni (II) complexes with imine-based ligands, J. Mol. Struct. 1247 (2022) 131351.
[94] P. Bhoopathy, K. Subramani, B.S. Krishnamoorty, Synthesis, structural characterization and biological applications of mono- and binuclear Cu(II) and Ni (II) complexes with N2O2 Schiff bases, Inorg. Chem. Commun. 166 (2024) 112583.
[95] J.M. Ramos, M.T. de M. Cruz, A.C. Costa Jr., G. F. Ondar, G.B. Ferreira, L. Raniero, A.A. Martin, O. Versiane, C.A.T. Soto, Molecular structure, natural bond analysis, vibrational, and electronic spectra of aspartateguanidoacetatenickel(II), [Ni(Asp)(GAA)]·H2O: DFT quantum mechanical calculations, Spectrochim. Acta A Mol. Biomol. Spectrosc. 97 (2012) 1041-1051.
[96] K. Sarojini, H. Krishnan, C.C. Kanakam, S. Muthu, Synthesis, X-ray structural, characterization, NBO and HOMO–LUMO analysis using DFT study of 4-methyl-N-(naphthalene-1-yl)benzene sulfonamide, Spectrochim. Acta A Mol. Biomol. Spectrosc. 96 (2012) 657–667.
[97] R. Vasanthakumari, W. Nirmala, S. Sagadevan, S. Mugeshini, N. Rajeswari, R. Balu, R. Santhakumari, Synthesis, growth, crystal structure, vibrational, DFT and HOMO, LUMO analysis on protonated molecule-4-aminopyridinium nicotinate, J. Mol. Struct. 1239 (2021) 130449.
[98] A.M. Abu-Dief, T. El-Dabea, R.M. El-Khatib, A. Abdou, I.O. Barnawi, H.A. H. Alshehri, K. Al-Ghamdi, M.A.E.A.A.A. El-Remaily, Fabrication, physicochemical characterization and theoretical studies of some new mixed ligands complexes based on N-(1H-benzimidazol-2-yl)-guanidine and 1, 10-phenanthroline: DNA interaction, biological applications and molecular docking approach, J. Mol. Struct. 1310 (2024) 138328.
[99] B. Sureshkumar, Y.S. Mary, S. Suma, S. Armaković, S.J. Armaković, C.V. Alsenay, B. Narayana, B.P. Sasidharan, Spectroscopic characterization of 8-hydroxy-5-nitroquinoline and 5-chloro-8-hydroxy quinoline and investigation of its reactive properties by DFT calculations and molecular dynamics simulations, J. Mol. Struct. 1164 (2018) 525–538.
[100] S. Celik, S. Yurdakul, B. Erdem, New silver(I) complex as antibiotic candidate: Synthesis, spectral characterization, DFT, QTAIM and antibacterial investigations and docking properties, J. Mol. Struct. 1261 (2022) 132902.
[101] E. Barim, F. Akman, Synthesis, characterization and spectroscopic investigation of N-(2-acetylbenzofuran-3-yl)acrylamide monomer: Molecular structure, HOMO-LUMO study, TD-DFT and MEP analysis, J. Mol. Struct. 1195 (2019) 506–513.
[102] S. Zinatloo-Ajabshir, S. Rakhshani, Z. Mehrabadi, M. Farsadrooh, M. FeiziDehnayebi, S. Rakhshani, M. Dušek, V. Eigner, S. Rtimi, T. M. Aminabhavi, Novel rod-like [Cu (phen)$_2$(OAc)]·PF$_6$ complex for high-performance visible-light-driven photocatalytic degradation of hazardous organic dyes: DFT approach, Hirshfeld and fingerprint plot analysis, J. Environ. Manage. 350 (2024) 119545.
[103] S. Celik, S. Yurdakul, B. Erdem, Synthesis, spectroscopic characterization (FT-IR, PL), DFT calculations and antibacterial activity of silver(I) nitrate complex with nicotinaldehyde, Inorg. Chem. Commun. 131 (2021) 108760.
[104] S. Murugavel, V.V. Velan, D. Kannan, M. Bakthadoss, Synthesis, crystal structure analysis, spectral investigations, DFT computations, biological activities and molecular docking of methyl(2E)-2-{[N-(2-formlyphenyl)(4-metylbrnzene) sulfonamido]metyl}-3-(4-flurophenyl)prop-2enoate, a potential bioactive agent, J. Mol. Struct. 1108 (2016) 150–167.
[105] F.C. Asogwa, E.C. Agwamba, H. Louis, M.C. Muozie, I. Benjamin, T.E. Gber, G. E. Mathias, A.S. Adeyinka, A.I. Ikeuba, Structural benchmarking, density functional theory simulation, spectroscopic investigation and molecular docking of N-(1H-pyrrol-2-yl)methylene)-4-methylaniline as castration-resistant prostate cancer chemotherapeutic agent, Chem. Phys. Impact 5 (2022) 100091.
[106] A. Sethi, R.P. Singh, D. Shukla, P. Singh, Synthesis of novel pregnane-diosgenin prodrugs via Ring A and Ring A connection: a combined experimental and theoretical studies, J. Mol. Struct. 1125 (2016) 616–623.
[107] B.Q. Sheeba, M.S.M. Mary, M. Amalanathan, C.B. Job, Structural and vibrational spectral investigation on the identification of non-linear optical properties and wave function analyses (electrostatic potential, electron localisation function, localised orbital locator) of 3-ethoxy salicilaldehyde, Mol. Simulat. 47 (15) (2021) 1217–1233.
[108] A. Ahsin, M. Kurbanova, S. Ahmad, A. Qamar, M. Ashfaq, M.N. Tahir, N. Dege, O. Şahin, H.A. Abuelizz, R. Al-Salahi, Y. El Bakri, Synthesis, structure, supramolecular assembly inspection by Hirshfeld surface analysis, DFT study and molecular docking inspection of 4,5-bis(2-chlorophenyl)-8a-phenylhexahydropyrimido[4,5-d]pyrimidine-2,7(1*H*,3*H*)-dithione, J. Mol. Struct. 1319 (2) (2025) 139580.
[109] E. Espinosa, E. Molins, C. Lecomte, Hydrogen bond strengths revealed by topological analyses of experimentally observed electron densities, Chem. Phys. Lett. 285 (1998) 170–173.
[110] M. Medimagh, N. Issaoui, S. Gatfaoui, S.A. Brandan, O. Al-Dossary, H. Marouani, M.J. Wojcik, Impact of non-covalent interactions on FT-IR spectrum and properties of 4-methylbenzylammonium nitrate. A DFT and Molecular Docking Study, Heliyon 7 (2021) e08204.
[111] E.R. Johnson, S. Keinan, P. Mori-Sanchez, J. Contreras-García, A.J. Cohen, W. Yang, Revealing noncovalent interactions, J. Am. Chem. Soc. 132 (2010) 6498–6506.
[112] R. Suja, A. Rathika, V.S.J. Reeda, A.A. Kumar, P. Divya, Synthesis, spectroscopic analysis (FT-IR, FT-Raman, UV, NMR), non-covalent interactions (RDG, IGM) and dynamic simulation on bis(8-hydroxy quinoline) salicylate salicylic acid, J. Mol. Struct. 1310 (2024) 138231.
[113] S.B. Radder, R. Melavanki, U. Radder, S.M. Hiremathc, R. Kusanur, S. S. Khemalapuree, Synthesis, spectroscopic (FT-IR, FT-Raman, NMR), reactivity (ELF, LOL and Fukui) and docking studies on 3-(2–hydroxy-3–methoxy-phenyl) -1-(3-nitro-phenyl)-propenone by experimental and DFT methods, J. Mol. Struct. 1255 (2022) 132443.
[114] A.D. Steffy, D.A. Dhas, I.H. Joe, S. Balachandran, Theoretical investigations on structural, spectral, NBO, NLO and topology exploration (AIM, ELF, LOL, RDG) of piperazine-2,5-dione oxalic acid monohydrate, J. Mol. Struct. 1295 (2024) 136653.
[115] A.M. Khedr, H.A. El-Ghamry, K.M. Wahdan, H.S.A. Mandour, Synthesis, characterization, antimicrobial, molecular docking simulation, and antitumor assays of nanometric complexes based on new thiazole Schiff base derivative, Appl. Organomet. Chem. 38 (2024) 7362.
[116] M.M. Khalaf, H.M.A. El-Lateef, M. Gouda, A.A. Amer, A.A. Abdelhamid, M.F. A. Taleb, A. Alfarsi, T.M.A. Ibrahim, H. El-Shamy, A. Abdou, Synthesis, characterization, DFT, biological activity evaluation, and molecular docking analysis of new 8-[(2-hydroxynaphthalen-1-yl)diazenyl] naphthalene-1,3-disulfonic acid based complexes, J. Mol. Struct. 1300 (2024) 137175.
[117] M. Yadav, D. Yadav, S. Kansal, A. Angrup, N. Taneja, D.P. Singh, J.K. Kapoor, Pharmacologically important tetraaza macrocyclic Schiff base complexes of Zn (II), Cu(II) and Co(II): Synthesis, characterization, DFT studies, molecular docking and in vitro anti-bacterial and anti-cancer studies, J. Mol. Struct. 1317 (2024) 139078.
[118] A.M. Abbas, H.A. Salem, A.S. Orabi, Synthesis, characterization, in vitro and in silico assessment of novel diclofenac derivative metal complexes, J. Mol. Struct. 1318 (2024) 139191.
[119] M.A. Syabana, N.D. Yuliana, I. Batubara, D. Fardiaz, α-glucosidase inhibitors from Syzygium polyanthum (Wight) Walp leaves as revealed by metabolomics and in silico approaches, J. Ethnopharmacol. 282 (2022) 114618.

Ceyhun Kucuk Education:I completed my undergraduate education at Samsun Ondokuz Mayıs University, Faculty of Arts and Sciences, Department of Physics, in 2010. I completed my master's degree at Zonguldak Bülent Ecevit University, Institute of Science, Department of Nuclear Physics, and I have completed my doctorate at Gazi University, Institute of Science, Department of Atomic and Molecular Physics as of 2023. Research Topics: My research areas are the synthesis of organic and inorganic molecules, spectroscopic analysis, and DFT calculations, as well as the investigation of their biological activities. During and after my doctoral education, I have published in many important journals related to my field of study. Work Experience: I have been working as a lecturer at Zonguldak Bülent Ecevit University since 2017.